

NPSolver: Neural Poisson Solver with Iterative Physics Supervision

Bocheng Zeng*
Gaoling School of Artificial
Intelligence
Renmin University of China
Beijing, China
zengbocheng@ruc.edu.cn

Rui Zhang*
Gaoling School of Artificial
Intelligence
Renmin University of China
Beijing, China
rayzhang@ruc.edu.cn

Runze Mao
School of Mechanics and Engineering
Science
Peking University
Beijing, China
maorz1998@stu.pku.edu.cn

Mengtao Yan
Gaoling School of Artificial
Intelligence
Renmin University of China
Beijing, China
mengtaoyan@ruc.edu.cn

Xuan Bai
AI for Science Institute
Beijing, China
xuan.bai@pku.edu.cn

Yang Liu
School of Engineering Science
University of Chinese Academy of
Sciences
Beijing, China
liuyang22@ucas.ac.cn

Zhi X. Chen
School of Mechanics and Engineering
Science
Peking University
Beijing, China
chenzhi@pku.edu.cn

Hao Sun[†]
Gaoling School of Artificial
Intelligence
Renmin University of China
Beijing, China
haosun@ruc.edu.cn

Abstract

Efficiently solving Poisson equations on complex, irregular domains remains a fundamental challenge in scientific computing, as classical iterative solvers often suffer from prohibitive runtime due to ill-conditioned systems. While neural operators offer a fast alternative, they typically rely on large-scale labeled datasets or struggle with unstable training dynamics when using physics-informed residual losses. We propose NPSOLVER, a neural Poisson solver trained without solution labels via iterative physics supervision. Instead of relying on fully converged numerical solutions or raw PDE residuals, NPSOLVER utilizes a small number of preconditioned conjugate gradient (PCG) steps to refine its own predictions, providing a more stable and well-scaled training signal. Theoretical analysis confirms that this iterative supervision serves as a well-conditioned error proxy and that a stop-gradient design is essential for optimization stability. To better capture boundary-driven features under mixed boundary conditions, we further introduce the Boundary-Aware Transolver (BA-TRANSOLVER) architecture that explicitly separates interior and boundary tokenization. Extensive evaluations on 2D and 3D irregular geometries demonstrate that NPSOLVER outperforms both physics-informed and data-driven

baselines. Furthermore, a downstream thermal control task highlights the model's capability for conducting efficient and reliable gradient-based boundary control. We will release our codes and data at <https://github.com/intell-sci-comput/NPSolver>.

CCS Concepts

• **Computing methodologies** → **Artificial intelligence**; **Modeling and simulation**; • **Applied computing** → *Physics*.

Keywords

Poisson equation, Neural PDE solver, Iterative physics supervision, Physics-informed machine learning, Surrogate modeling

ACM Reference Format:

Bocheng Zeng, Rui Zhang, Runze Mao, Mengtao Yan, Xuan Bai, Yang Liu, Zhi X. Chen, and Hao Sun. 2026. NPSolver: Neural Poisson Solver with Iterative Physics Supervision. In *Proceedings of the 32nd ACM SIGKDD Conference on Knowledge Discovery and Data Mining V.2 (KDD '26)*, August 09–13, 2026, Jeju Island, Republic of Korea. ACM, New York, NY, USA, 16 pages. <https://doi.org/10.1145/3770855.3818906>

1 Introduction

Efficiently solving Poisson equations on complex and irregular domains remains a major computational bottleneck in many scientific and engineering pipelines. As a cornerstone PDE, the Poisson operator underlies a wide range of physical processes, including pressure projection in incompressible flows [3], steady-state heat conduction [28], and electrostatics [10]. Classical methods discretize the PDE using numerical schemes such as finite volumes [26], finite elements [49], or finite differences [15], resulting in a large, sparse linear system solved by iterative methods, e.g., preconditioned

*Equal contributions.

[†]Corresponding author.



conjugate gradient (PCG) [8, 35] or multigrid [2, 38]. While these solvers are robust, their runtime is dominated by the iteration count, which increases sharply for irregular geometries and challenging boundary conditions (BCs) that induce ill-conditioned systems.

To accelerate classical solvers, learning-based approaches have emerged as a promising alternative, using neural networks as fast surrogate models. This paradigm includes operator-learning methods [18, 23, 31, 37, 39] trained on paired input–solution data, as well as graph- and transformer-based surrogates [19, 25, 43] that better handle irregular meshes and unstructured grids. Despite their fast inference, most such methods rely on large collections of ground-truth solutions generated by expensive numerical solvers, which can be prohibitive for complex geometries and diverse BCs.

To reduce the dependence on labeled data, Physics-Informed Neural Networks (PINNs) [11, 32, 44] replace data supervision with physics losses, e.g., PDE residuals and boundary constraints. However, optimizing physics-informed objectives is often unstable and costly in practice. On the one hand, PINNs can struggle with stiff operators and ill-conditioned regimes, leading to slow convergence and high sensitivity to hyperparameters [14, 42]. On the other hand, PINNs typically require per-instance optimization, necessitating retraining when the domain geometry or BCs change [6]. Recent physics-informed operator learning methods [22, 41, 47] further extend this idea by using physics supervision to train neural operators, thereby avoiding the per-instance retraining like PINNs. However, these methods still rely on residual-based objectives (strong-form residuals via automatic differentiation [41] or discretized PDE residuals [22]), where gradients can be poorly scaled in stiff or ill-conditioned regimes, leading to slow convergence and unstable training dynamics. Moreover, many existing approaches are developed under regular-grid backbones and simple geometry, which limits their ability to generalize across BCs and complex, irregular domains.

We propose NPSOLVER, a neural Poisson solver trained *without* solution labels via iterative physics supervision. During training, NPSOLVER applies a small number (K) of PCG steps to the network prediction and uses the PCG-updated iterate as the supervision target. This bypasses the need for fully converged numerical labels that typically require T iterations, where $K \ll T$. Compared with physics-informed methods that directly minimize PDE residuals, NPSOLVER adopts iterative physics supervision, which provides a more stable and well-scaled training signal. We further provide theoretical guarantees showing that the induced self-consistency residual is a well-conditioned error proxy and that the stop-gradient design yields more favorable optimization dynamics. For architecture design, to improve generalization across domain geometries and BCs, we introduce a Boundary-Aware Transolver variant (BA-TRANSOLVER) that can handle various boundary-value problems on irregular meshes. BA-Transolver separately tokenizes interior and boundary nodes and performs attention over the combined token set to explicitly model complex boundary–interior interactions.

We validate NPSOLVER on three challenging settings: (i) 2D Poisson problems on irregular domains with varying forcing fields and boundary regimes, (ii) 3D Poisson problems on a cube-with-cylindrical-hole family, and (iii) a downstream thermal control task on a perforated plate. We evaluate both *in-distribution* accuracy and *out-of-distribution* generalization under geometry shifts

and boundary-condition changes. In the most challenging RandomBC regime, NPSOLVER achieves **8.17%** relative L_2 error without any paired labels, outperforming the strongest supervised baseline trained with **7k** labeled samples (**10.17%**). Moreover, it delivers a **15×** speedup at matched accuracy compared with classical numerical methods. In summary, we make the following contributions:

1. We present NPSOLVER, a label-free neural Poisson solver built on BA-TRANSOLVER, a boundary-aware attention model designed to handle complex BCs. NPSOLVER is trained with an iterative physics supervision objective, avoiding the cost of generating fully converged solution pairs.

2. We provide theoretical guarantees for iterative physics supervision. The induced self-consistency residual is a well-conditioned error proxy, and the stop-gradient design leads to more stable and well-scaled training than directly minimizing PDE residuals.

3. We conduct comprehensive evaluations in 2D and 3D irregular domains, and a downstream control task, demonstrating that NPSOLVER offers a favorable error–cost trade-off and strong *out-of-distribution* generalization for Poisson equations.

2 Related Work

Supervised neural surrogates. Given enough training data, a prominent research direction involves learning solution operators in a data-driven manner. Neural operator models, such as FNO [18], DeepONet [23], and their invariants [17, 24, 37], learn direct mappings from problem inputs to solution fields and have demonstrated strong performance across benchmark PDE families. To handle irregular geometries and unstructured discretizations, graph-based and geometric models [19, 21, 29, 45] operate directly on meshes or point clouds. Transformer-based surrogates [7, 20, 25, 43] leverage attention mechanisms to model global interactions within the solution domain. Despite their inference speed, these supervised approaches typically require massive datasets of paired solution labels generated by high-fidelity numerical solvers.

Physics-informed learning. Classical Physics-Informed Neural Networks (PINNs) and their variants [11, 32, 33, 44] optimize networks by minimizing strong-form PDE residuals alongside boundary condition penalties. While these have shown promising results across various physical systems, a complementary family of approaches [4, 12, 13, 36] leverages weak forms or variational principles to improve training stability and reduce sensitivity to higher-order derivatives. Despite being label-free, these physics-informed methods are typically optimized per instance, i.e., requiring a separate optimization process for each new problem configuration. To develop reusable neural solvers, physics-informed operator methods combine operator learning with physics-based objectives [16, 22, 41, 47, 48], aiming for operator-level generalization. However, many current physics-informed operator frameworks still rely on regular-grid backbones or assume fixed geometries. This reliance hinders their direct application and limits their ability to generalize to irregular domains.

Learning-based iterative solvers. A distinct line of research aims to reduce the computational cost of iterative algorithms by learning specialized update rules or integrating neural predictors with classical solvers. LISTA [5] learns a finite sequence of iterative updates by unrolling an optimization algorithm into neural layers, while

implicit fixed-point models like DEQ [1] define networks via equilibrium equations solved through root-finding during inference. For PDEs, Hsieh et al. learn neural modifications to iterative solvers that maintain convergence guarantees, and HINTS [46] blends neural operators with relaxation methods to refine solutions iteratively. In contrast, we run a small number of PCG steps only during training to generate physics self-supervision targets, producing predictions in a single forward pass during inference.

3 Methods

3.1 Problem Formulation

We consider the Poisson equation in $d \in \{2, 3\}$ spatial dimensions on a computational domain $\Omega \subset \mathbb{R}^d$ bounded by $\partial\Omega$. Given a forcing field $f : \Omega \rightarrow \mathbb{R}$, a Poisson solver aims to find a scalar field $u : \Omega \rightarrow \mathbb{R}$ such that

$$\begin{aligned} \nabla^2 u(\mathbf{x}) &= f(\mathbf{x}), & \mathbf{x} \in \Omega, \\ \mathcal{B}(u)(\mathbf{x}) &= g(\mathbf{x}), & \mathbf{x} \in \partial\Omega \end{aligned} \quad (1)$$

where \mathcal{B} denotes the boundary operator. In this work, we focus on Dirichlet and Neumann boundary conditions (BCs). Specifically, we prescribe $u(\mathbf{x}) = g_D(\mathbf{x})$, $\mathbf{x} \in \partial\Omega_D$ and $\frac{\partial u}{\partial \mathbf{n}}(\mathbf{x}) = g_N(\mathbf{x})$, $\mathbf{x} \in \partial\Omega_N$ with $\partial\Omega = \partial\Omega_D \cup \partial\Omega_N$ and $\partial\Omega_D \cap \partial\Omega_N = \emptyset$, with \mathbf{n} representing the outward unit normal.

To obtain a discrete numerical solution, we discretize the domain and the governing equation using a cell-centered finite volume method (FVM). As illustrated in Fig. 1, the domain Ω is partitioned into a set of control volumes $\{V_i\}_{i=1}^N$, where the primary unknowns are stored at the corresponding cell centroids $\{\mathbf{x}_i\}_{i=1}^N \in \Omega$. BCs are imposed at the boundary-face centroids $\{\mathbf{y}_i\}_{i=1}^{N_b} \in \partial\Omega$. Applying the finite-volume integration and standard flux approximations transforms the continuous PDE into a sparse linear system:

$$\mathbf{A}\mathbf{u} = \mathbf{b} \quad (2)$$

where $\mathbf{u} \in \mathbb{R}^N$ is the vector of discrete cell-centered solutions, $\mathbf{A} \in \mathbb{R}^{N \times N}$ is the discrete Laplacian operator (incorporating mesh geometry and boundary treatment), and $\mathbf{b} \in \mathbb{R}^N$ aggregates the contributions from the source term f and the boundary data g . The resulting sparse system is typically solved using an iterative Preconditioned Conjugate Gradient (PCG) method, which often requires hundreds or thousands of iterations to reach full convergence.

In this paper, we aim to learn a neural solution operator \mathcal{N}_θ that maps the domain geometry Ω , boundary condition B , and the forcing field f directly to the corresponding solution field, i.e.,

$$\mathcal{N}_\theta : (\Omega, B, f) \mapsto \mathbf{u}. \quad (3)$$

3.2 The Overview of NPSOLVER

We propose NPSOLVER, a label-free neural Poisson solver trained via iterative physics supervision (Fig. 2). For each training instance,

we sample a triplet (Ω, B, f) on the fly, where Ω is a geometry, B is a boundary condition, and f is a forcing field. Given (Ω, B, f) , the network \mathcal{N}_θ predicts a cell-centered solution $\hat{\mathbf{u}}$. Unlike directly using PDE residual [22], NPSOLVER conducts K steps of PCG initialized at $\hat{\mathbf{u}}$ to obtain a self-supervision target $\tilde{\mathbf{u}} = F_K(\hat{\mathbf{u}})$, and minimizes $\|\hat{\mathbf{u}} - \tilde{\mathbf{u}}\|_2^2$ while stopping gradients through F_K . This objective enjoys stronger theoretical guarantees and alleviates the ill-conditioning issues that arise when directly minimizing the PDE residual (see Sec. 3.4). To improve generalization under irregular meshes and mixed BCs, we introduce a Boundary-Aware Transolver (BA-TRANSOLVER). Unlike TRANSOLVER [43], BA-TRANSOLVER tokenizes interior and boundary nodes separately and performs attention jointly, which improves modeling under mixed BCs and geometry shifts through boundary–interior interactions (Sec. 3.3).

3.3 Model Architecture

Our network architecture (BA-TRANSOLVER) follows an encoder-block-decoder design (Fig. 2). The encoder maps physical inputs to latent node embeddings, a stack of L Boundary-Aware (BA) blocks performs global message passing in a compact token space, and the decoder projects the updated embeddings back to the solution.

The core innovation is the Boundary-Aware Attention module within each BA block. This module extends the "physics-attention" mechanism of TRANSOLVER [43] by introducing two separate token streams. Unlike the original TRANSOLVER, which applies a shared slicing operation across all nodes, our approach separately tokenizes interior and boundary nodes before performing attention over their concatenation. This explicitly exposes boundary information in the token space, significantly improving sensitivity to mixed BCs and geometric shifts.

Given a cell-centered finite-volume mesh of domain Ω , we define interior nodes $\{\mathbf{x}_i\}_{i=1}^N$ at cell centroids and boundary nodes $\{\mathbf{y}_j\}_{j=1}^{N_b}$ at boundary-face centroids. We construct interior node features \mathbf{p}_i from spatial coordinates, and the forcing f , and boundary node features \mathbf{q}_j from spatial coordinates, BC type, and the prescribed values. The initial stage of the BA-TRANSOLVER involves mapping physical features into a latent space while maintaining the distinction between the domain interior and its boundaries. Two encoders produce interior embeddings $\mathbf{h}_i^{\text{int}} = \text{Enc}_{\text{int}}(\mathbf{p}_i)$ and boundary embeddings $\mathbf{h}_j^{\text{bd}} = \text{Enc}_{\text{bd}}(\mathbf{q}_j)$, respectively. Collecting these embeddings into matrices $\mathbf{H}_{\text{int}} \in \mathbb{R}^{N \times d}$ and $\mathbf{H}_{\text{bd}} \in \mathbb{R}^{N_b \times d}$, we learn two sets of slice-assignment weights for interior and boundary nodes, $\mathbf{W}_{\text{int}} \in \mathbb{R}^{N \times S_{\text{int}}}$ and $\mathbf{W}_{\text{bd}} \in \mathbb{R}^{N_b \times S_{\text{bd}}}$, via two separate projection heads:

$$\mathbf{W}_{\text{int}} = \text{Softmax}(\Phi_{\text{int}}(\mathbf{H}_{\text{int}})), \quad \mathbf{W}_{\text{bd}} = \text{Softmax}(\Phi_{\text{bd}}(\mathbf{H}_{\text{bd}})), \quad (4)$$

where the softmax is applied along the slice dimension. This dual-stream approach ensures that boundary information is not overlooked by the much larger number of interior nodes. Using these assignments, we aggregate node embeddings into slice tokens by weighted pooling:

$$\mathbf{Z}_{\text{int}} = \text{Pooling}(\mathbf{W}_{\text{int}}, \mathbf{H}_{\text{int}}), \quad \mathbf{Z}_{\text{bd}} = \text{Pooling}(\mathbf{W}_{\text{bd}}, \mathbf{H}_{\text{bd}}) \quad (5)$$

where $\text{Pooling}(\mathbf{W}, \mathbf{H})$ denotes normalized weighted sums over nodes. We concatenate the two token sets and apply multi-head

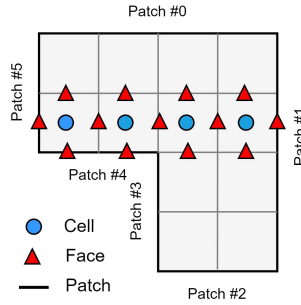


Figure 1: Cell-centered FVM mesh: cell, face, and patch.

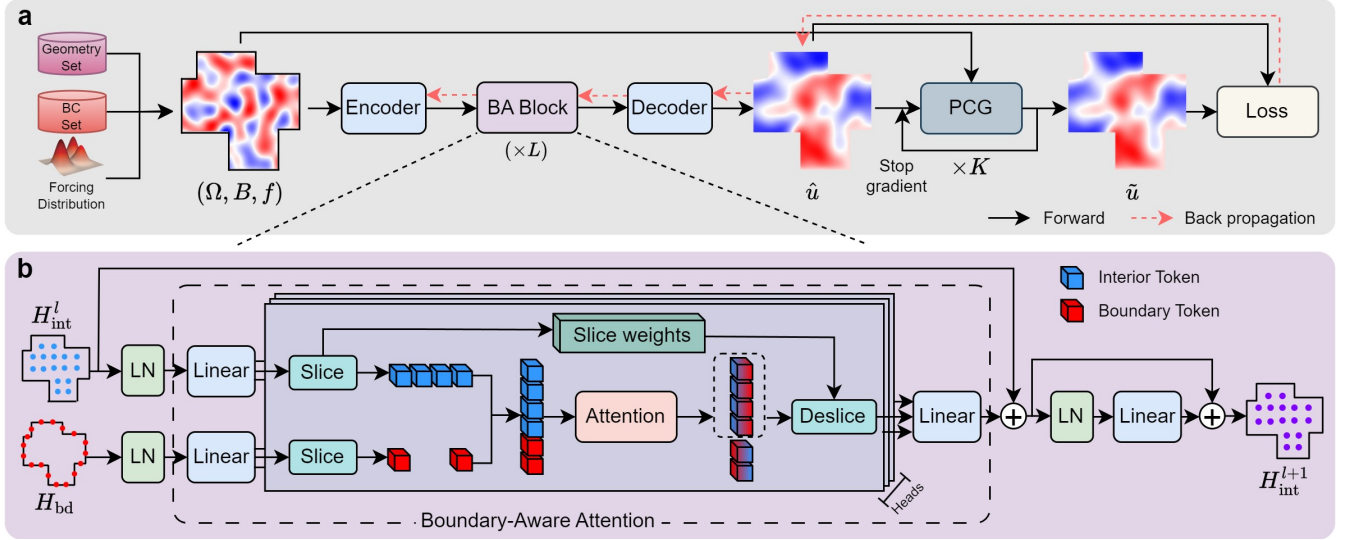


Figure 2: Overview of NPSOLVER. (a) Iterative Physics Supervision: The network predicts \hat{u} for a sampled instance (Ω, B, f) , which is refined by K PCG steps to generate a self-supervision target \tilde{u} (with stop-gradient). **(b) BA-TRANSOLVER Architecture:** Interior and boundary nodes are respectively tokenized into Z_{int} , Z_{bd} and attended jointly to model boundary-interior interactions.

self-attention (MHA) to achieve boundary–interior interactions:

$$Z = [Z_{int}; Z_{bd}], \quad Z' = \text{MHA}(Z). \quad (6)$$

Finally, we update only the interior node embeddings by deslicing from the updated interior tokens Z'_{int} :

$$H'_{int} = \text{Deslice}(W_{int}, Z'_{int}). \quad (7)$$

In this design, boundary tokens act as a persistent conditioning context. They inject boundary information into the global interactions while keeping the boundary representation anchored to the prescribed BCs. Each BA block follows a pre-norm transformer structure with residual connections and a feed-forward layer.

3.4 Iterative Physics Supervision

As described in Sec. 3.1, our numerical reference pipeline discretizes the Poisson problem via a cell-centered FVM, yielding a sparse linear system $\mathbf{A}\mathbf{u} = \mathbf{b}$. While solutions are obtainable using an iterative PCG solver, challenging geometries often require a large number of iterations to satisfy strict convergence tolerances. We exploit this discretize-solve workflow to construct a physics supervision signal that requires only a small number of iterative steps during training.

Given an instance (Ω, B, f) , the network predicts a cell-centered field $\hat{\mathbf{u}} = \mathcal{N}_\theta(\Omega, B, f)$. Rather than supervising $\hat{\mathbf{u}}$ with a computationally expensive converged label, we run K steps of PCG initialized at $\hat{\mathbf{u}}$, and denote the resulting K -step update operator by $F_K(\cdot)$. We treat the K -step iterate as a pseudo-label,

$$\tilde{\mathbf{u}} = \text{sg}(F_K(\hat{\mathbf{u}})), \quad (8)$$

where $\text{sg}(\cdot)$ denotes the stop-gradient operator. The model is trained by minimizing the discrepancy between the prediction and its PCG-updated counterpart:

$$L_{\text{iter}}(\theta) = \|\hat{\mathbf{u}} - \tilde{\mathbf{u}}\|_2^2. \quad (9)$$

During training, PCG acts purely as a target generator, where gradients are not propagated through $F_K(\cdot)$, and backpropagation is performed only through the neural network.

Minimizing L_{iter} enforces a self-consistency condition induced by the iterative solver, i.e., $\hat{\mathbf{u}} \approx F_K(\hat{\mathbf{u}})$. Near convergence, additional PCG steps produce only small corrections; conversely, when $\hat{\mathbf{u}}$ is far from satisfying $\mathbf{A}\mathbf{u} = \mathbf{b}$, the PCG update provides a nontrivial, physics-consistent correction direction. In this way, iterative physics supervision trains the network to output a state that is already close to the converged solution in a single forward pass, amortizing a substantial portion of the iterative solve into inference.

One common physics-informed baseline directly minimizes the discrete residual, e.g., $L_{\text{res}} = \|\mathbf{A}\hat{\mathbf{u}} - \mathbf{b}\|$. In our setting, \mathbf{A} can be ill-conditioned on irregular meshes, making residual-based optimization slow and unstable due to poorly scaled gradients. In contrast, L_{iter} learns from the solver’s update in the solution space, which implicitly incorporates the effect of preconditioning and yields a more effective training signal toward the converged manifold. We analyze these properties theoretically in Sec. 4 and validate them empirically in Sec. 5.4.

Although we instantiate iterative supervision with PCG in the Poisson/SPD setting, the high-level idea only requires a truncated solver map F_K . In principle, F_K could be replaced by other Krylov solvers matched to the algebraic structure of the system, such as GMRES or MINRES, although our current theory is specific to the SPD case. We use a Jacobi preconditioner in this work because it is simple, cheap, and robust on varying irregular meshes, which helps isolate the effect of iterative supervision itself. Stronger SPD preconditioners may further improve conditioning and reduce the required K , but they also introduce additional setup cost and solver-specific complexity.

4 Theory

This section establishes three theoretical results: (i) fixed-point consistency of the PCG- K map, (ii) the analysis of stop-gradient, and (iii) the self-consistency residual is a well-conditioned error proxy. All proofs are provided in Appendix C.

4.1 Setup

After discretization, each Poisson equation yields a linear system $\mathbf{A}\mathbf{u} = \mathbf{b}$. Throughout this section, we assume:

- (A1) \mathbf{A} is symmetric positive definite (SPD);
- (A2) the preconditioner \mathbf{M} used by PCG is SPD.

Define the self-consistency residual $\mathbf{s}_K(\mathbf{u}) := \mathbf{u} - F_K(\mathbf{u})$. Let $\mathbf{u}^* := \mathbf{A}^{-1}\mathbf{b}$ be the unique solution. For SPD \mathbf{A} , define the energy norm $\|\mathbf{x}\|_A := \sqrt{\mathbf{x}^\top \mathbf{A} \mathbf{x}}$. Define the preconditioned matrix $\mathbf{C} := \mathbf{M}^{-1/2} \mathbf{A} \mathbf{M}^{-1/2}$ and $\kappa := \kappa(\mathbf{C}) = \lambda_{\max}(\mathbf{C}) / \lambda_{\min}(\mathbf{C})$. Accordingly, let

$$\rho := \frac{\kappa - 1}{\kappa + 1} \in [0, 1). \quad (10)$$

4.2 Fixed-point Consistency

A basic concern for solver-induced self-supervision is whether the induced objective introduces spurious minimizers. The following result shows that the only fixed points of the finite-iteration PCG map are exact solutions of the linear system.

THEOREM 4.1. *Assume A1–A2 and $K \geq 1$. Then for any $\mathbf{u} \in \mathbb{R}^N$,*

$$F_K(\mathbf{u}) = \mathbf{u} \iff \mathbf{A}\mathbf{u} = \mathbf{b}. \quad (11)$$

4.3 Analysis of the Stop-gradient Update

Our objective uses PCG as a target generator and blocks gradients through F_K . To clarify why this matters, consider optimizing \mathbf{u} directly using the iterative physics residual $\mathbf{s}_K(\mathbf{u}) = \mathbf{u} - F_K(\mathbf{u})$. The stop-gradient training corresponds to the semi-gradient update $\mathbf{u}_{t+1} = \mathbf{u}_t - \eta \mathbf{s}_K(\mathbf{u}_t)$, which equals a relaxed fixed-point iteration.

THEOREM 4.2. *Assume A1–A2 and $K \geq 1$. Consider the iteration*

$$\mathbf{u}_{t+1} = \mathbf{u}_t - \eta \mathbf{s}_K(\mathbf{u}_t) = (1 - \eta)\mathbf{u}_t + \eta F_K(\mathbf{u}_t), \quad \eta \in (0, 1].$$

Let $\mathbf{e}_t = \mathbf{u}_t - \mathbf{u}^*$. Then

$$\|\mathbf{e}_{t+1}\|_A \leq (1 - \eta(1 - \rho^K)) \|\mathbf{e}_t\|_A.$$

REMARK 1. *The theorem establishes a global contraction guarantee for the stop-gradient dynamics. Furthermore, if a solver map F_K is differentiable at \mathbf{u}^* with Jacobian $\mathbf{J} = \nabla F_K(\mathbf{u}^*)$, then for the stop-gradient update we have*

$$\mathbf{e}_{t+1} = ((1 - \eta)\mathbf{I} + \eta\mathbf{J})\mathbf{e}_t + O(\|\mathbf{e}_t\|_2^2),$$

and for the full-gradient update on $\phi(\mathbf{u}) = \frac{1}{2} \|\mathbf{s}_K(\mathbf{u})\|_2^2$,

$$\mathbf{e}_{t+1} = \left(\mathbf{I} - \eta(\mathbf{I} - \mathbf{J})^\top (\mathbf{I} - \mathbf{J}) \right) \mathbf{e}_t + O(\|\mathbf{e}_t\|_2^2).$$

Therefore, the full-gradient direction multiplies the residual by an extra factor $(\mathbf{I} - \mathbf{J})^\top$, yielding an effective curvature $(\mathbf{I} - \mathbf{J})^\top (\mathbf{I} - \mathbf{J})$. When F_K is close to identity near \mathbf{u}^* (so that $\mathbf{J} \approx \mathbf{I}$), this can make the full-gradient step much weaker and more sensitive to the step size.

4.4 A Well-conditioned Error Proxy

The following theorem provides a uniform equivalence between $\|\mathbf{u} - F_K(\mathbf{u})\|_A$ and the energy error $\|\mathbf{u} - \mathbf{u}^*\|_A$, and contrasts it with the scaling behavior of the PDE residual $\mathbf{r}(\mathbf{u}) = \mathbf{A}\mathbf{u} - \mathbf{b}$.

THEOREM 4.3. *Assume A1–A2 and $K \geq 1$. Then for any \mathbf{u} ,*

$$(1 - \rho^K) \|\mathbf{u} - \mathbf{u}^*\|_A \leq \|\mathbf{s}_K(\mathbf{u})\|_A \leq (1 + \rho^K) \|\mathbf{u} - \mathbf{u}^*\|_A. \quad (12)$$

Furthermore, let $\mathbf{r}(\mathbf{u}) := \mathbf{A}\mathbf{u} - \mathbf{b}$. Then

$$\lambda_{\min}(\mathbf{A}) \|\mathbf{u} - \mathbf{u}^*\|_A \leq \|\mathbf{r}(\mathbf{u})\|_A \leq \lambda_{\max}(\mathbf{A}) \|\mathbf{u} - \mathbf{u}^*\|_A. \quad (13)$$

REMARK 2. *The theorem implies that $\|\mathbf{s}_K(\mathbf{u})\|_A$ tracks the true energy error $\|\mathbf{u} - \mathbf{u}^*\|_A$ up to a factor controlled by ρ^K ; hence it provides a well-scaled solution-space correction (especially when ρ^K is small). By contrast, the residual $\mathbf{A}\mathbf{u} - \mathbf{b}$ may be heavily rescaled by the spectrum of \mathbf{A} , and the squared-residual objective further suffers squared-conditioning since its curvature is \mathbf{A}^2 .*

5 Experiments

In this section, we present a comprehensive experimental evaluation of NPSOLVER to assess its performance under challenging domain geometries and BCs, including

- *2D generalization:* Tests on irregular domains to evaluate generalization across domain geometry, BCs, and forcing fields.
- *3D scalability:* Performance assessment on 3D domains with varying internal topologies and mixed BCs.
- *Downstream application:* Demonstration of NPSOLVER as a differentiable surrogate for gradient-based thermal control.
- *Efficiency and ablation:* Quantitative analysis of computational costs and various ablation studies.

NPSOLVER is trained with the iterative physics supervision and optimized with Adam and a OneCycle learning-rate schedule. We compare NPSOLVER against representative baselines spanning physics-informed and data-driven neural surrogates, including PI-DEEPONET [41], PINO [22], PINN [33], TRANSOLVER [43], TRANSOLVER++ [25], MGN [29], GPS [34], POINTNET++ [30], and BENO [40]. Ground-truth solutions are generated using an FVM coupled with a PCG solver. We report the relative L_2 error and inference time to assess model accuracy and computational cost.

5.1 2D Generalization under Different BCs

In this study, we evaluate NPSOLVER on 2D Poisson problems to assess generalization under domain geometries, BCs, and forcing fields. All models are trained on a fixed geometry distribution and tested on different domain geometries.

Geometry. Following BENO [40], we construct a corner-removed square family with five categories, denoted as C_k , where $k \in \{0, \dots, 4\}$ is the number of removed rectangular corners (C_0 corresponds to the intact square). For each domain geometry, the width and height of the removed corner rectangles are sampled independently from a uniform distribution (detailed in Appendix D.1). To evaluate both in-distribution and out-of-distribution generalization ability, we *train* the model only on the most irregular category C_4 and *test* it on all categories C_0 – C_4 .

BC regimes. We consider three boundary regimes, which define three cases that share the same geometry family and differ only in boundary specification: (i) **All-Dirichlet**, Dirichlet BCs with

Table 1: Relative L_2 error (%) and inference time (ms) across the various geometries (C4 to C0) in All-Dirichlet BCs.

Method	C4	C3	C2	C1	C0	Time
PI-DEEPONET	>100	>100	>100	>100	>100	56.5
PINO	19.40	23.67	23.88	25.46	26.53	5.5
PINN	<u>5.74</u>	<u>3.07</u>	<u>3.28</u>	1.13	0.77	251880
NPSOLVER	1.58	2.20	2.88	<u>3.34</u>	<u>3.59</u>	<u>9.1</u>

Table 2: Relative L_2 error (%) and inference time (ms) across the various geometries (C4 to C0) in All-Neumann BCs.

Method	C4	C3	C2	C1	C0	Time
PI-DEEPONET	>100	>100	>100	>100	>100	55.7
PINO	<u>34.66</u>	32.35	36.43	34.64	37.84	5.9
PINN	50.52	<u>27.25</u>	<u>11.74</u>	<u>24.79</u>	0.19	281860
NPSOLVER	3.11	4.62	7.95	11.27	<u>13.32</u>	<u>9.0</u>

zero value on all boundary patches; (ii) **All-Neumann**, zero-flux Neumann BCs on all boundary patches; and (iii) **RandomBC**, patch-wise mixed BCs where each boundary patch is independently and randomly assigned Dirichlet or Neumann type (each patch corresponds to a geometric segment, as illustrated in Fig. 1). Empirically, these cases exhibit increasing learning difficulty.

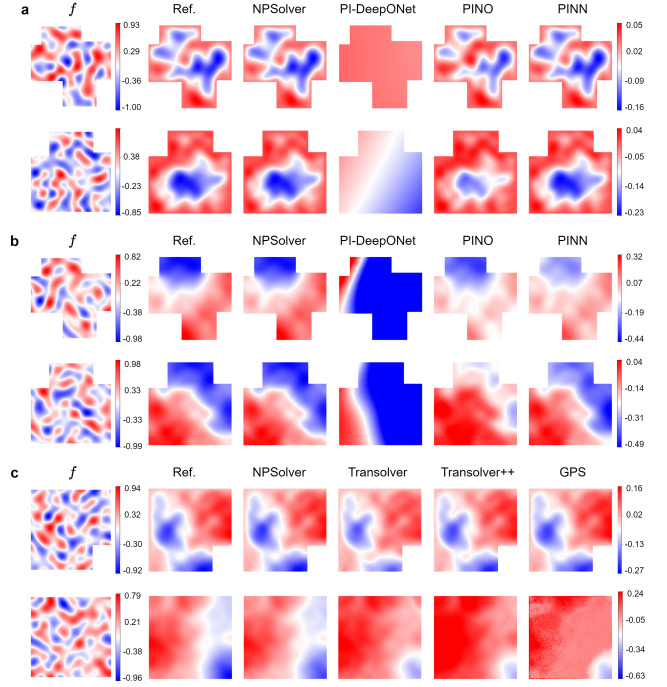
In each case, training samples (Ω, B, f) are generated on-the-fly by sampling a domain Ω from the above geometry set, assigning BCs B per the case definition, and drawing a forcing field f from the distribution (Appendix D.1). For evaluation, we generate 100 test samples per category, totaling 500 samples per case.

All-Dirichlet / Neumann results. In the All-Dirichlet and All-Neumann cases, we compare NPSOLVER against three representative self-supervised baselines, including PI-DEEPONET, PINO and PINN. Relative L_2 errors over the five geometry categories and average inference times are summarized in Table 1 and Table 2. Visualizations of models' predictions are provided in Fig. 3.

Notably, PI-DEEPONET implicitly assumes a fixed computational domain and struggles with joint generalization over both geometry and forcing. PINO, relying on an FNO backbone defined on regular grids, suffers from severe performance degradation under irregular geometry. PINN needs to retrain the network per sample, causing high optimization cost (Appendix D for further details).

Across both BC regimes, NPSOLVER consistently outperforms PI-DEEPONET and PINO by a wide margin. In the All-Dirichlet case, our accuracy is comparable to that of the per-instance PINN, while providing orders-of-magnitude faster inference at test time. In the more challenging All-Neumann case, NPSOLVER retains strong performance across geometry shifts and outperforms PINN on most categories. Overall, these results demonstrate that NPSOLVER delivers a favorable accuracy–efficiency trade-off, achieving robust generalization across domain geometry under both Dirichlet and Neumann BCs, while maintaining fast inference.

RandomBC results. In the RandomBC case, the model needs to simultaneously generalize across domain geometries, forcing fields, and patch-wise varying BCs. Given the limitations of the

**Figure 3: Visualization of models' predictions for representative samples. (a) All-Dirichlet case (C4 and C2). (b) All-Neumann case (C4 and C2). (c) RandomBC case (C1 and C0).**

three self-supervised baselines discussed above (e.g., fixed-domain assumptions, regular-grid constraints, and per-instance retraining), we instead compare NPSOLVER against representative data-driven baselines, including TRANSOLVER, TRANSOLVER++, MGN, GPS, POINTNET++, and BENO. For these baselines, we construct supervised datasets of varying sizes (e.g., 1k/3k/5k/7k labeled samples) for the C4 geometry category with the numerical solver. In contrast, NPSOLVER is trained without solution labels via iterative physics supervision (Appendix D for further details).

Fig. 4 illustrates the test error and training time as functions of training dataset size, with qualitative visualizations in Fig. 3(c). The reported training time for supervised baselines excludes the offline numerical label-generation cost. Remarkably, NPSOLVER achieves a relative L_2 error of 8.17% without any labeled data, outperforming the strongest data-driven baseline (10.17%) even when the latter is trained with 7k labeled samples. Furthermore, NPSOLVER requires significantly less training time than data-driven baselines. This highlights the efficiency of iterative physics supervision: it provides a stronger inductive bias and markedly better sample efficiency than purely data-driven regression, while avoiding the cost of large-scale label generation (More visualizations in Appendix Fig. A.2).

Computational cost. In the RandomBC case, we assess the practical utility of NPSOLVER via a multi-objective analysis of predictive accuracy, inference time, and GPU memory usage. All measurements are conducted on identical GPU hardware to ensure a fair comparison. As shown in Fig. 5(a), NPSOLVER occupies the optimal lower-left region, simultaneously achieving the lowest error and

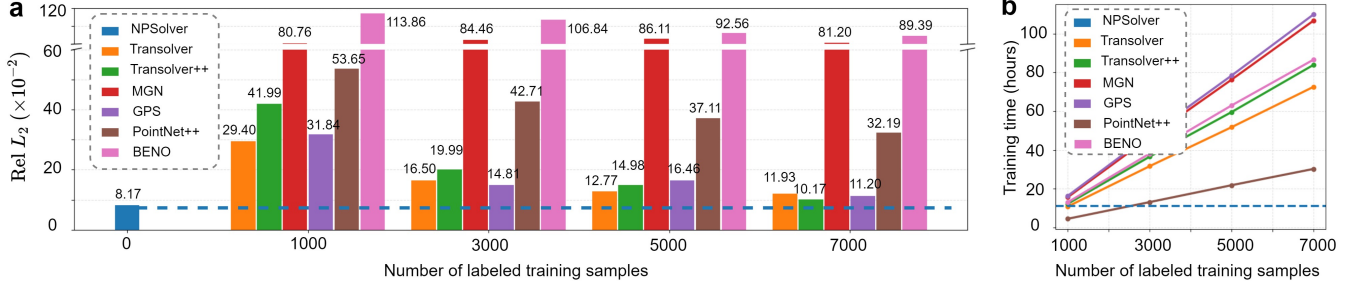


Figure 4: Data efficiency and scaling analysis in the RandomBC case. (a) Mean relative L_2 error as a function of the number of labeled training samples for supervised data-driven baselines trained on the C4 geometry category and NPSOLVER is trained without solution labels. (b) Comparison of training time under the same labeled-data budgets.

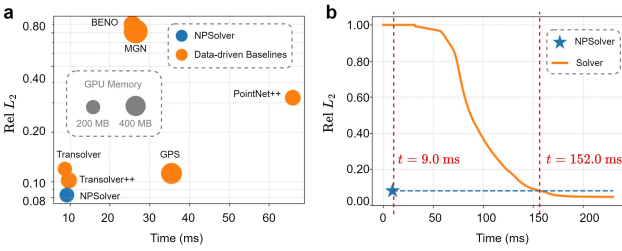


Figure 5: Computational Efficiency in the RandomBC case. (a) Multi-objective comparison of predictive accuracy, inference time, and GPU memory usage. (b) Accuracy–time comparison between NPSOLVER and the iterative numerical solver.

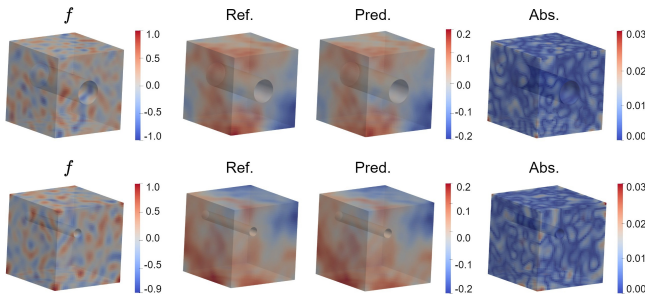


Figure 6: Representative 3D predictions of NPSOLVER on the cube-with-cylindrical-hole Poisson problem with mixed BCs.

high-speed inference with minimal memory overhead. To quantify the acceleration, we compare NPSOLVER against the iterative numerical solver. As illustrated in Fig. 5(b), NPSOLVER generates high-fidelity predictions in a single 9.0 ms forward pass, reaching an error level that the numerical solver attains after 152.0 ms. This represents an over 15× speedup at matched accuracy. These results highlight NPSOLVER’s robust generalization and its potential to serve as a high-efficiency alternative to classical iterative methods.

5.2 3D Poisson on Cube-with-Cylindrical-Hole

In this section, we evaluate the scalability of NPSOLVER on a 3D Poisson problem posed on irregular domains with mixed BCs. The task requires the model to generalize over both forcing fields and a parameterized family of geometries with internal cavities.

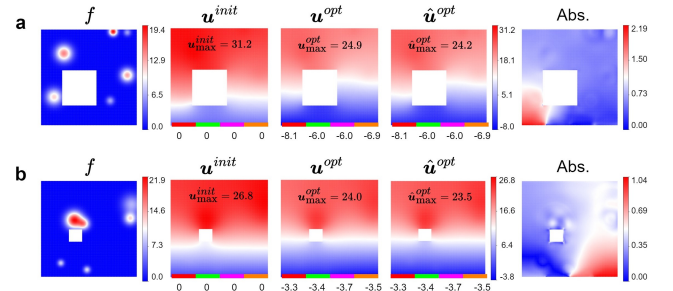


Figure 7: Visualization of the thermal control task of representative samples with forcing field f , the initial temperature u^{init} ($c = 0$), the reference temperature u^{opt} and NPSOLVER’s prediction \hat{u}^{opt} under optimized boundary values c .

Geometry and BCs. We construct a family of 3D domain geometries by subtracting a cylindrical cavity from a cube. Both the diameter d and the center position of the cylinder are randomly sampled (detailed in Appendix D.2). Regarding BCs, we impose zero-flux Neumann BCs on the outer cube surfaces, and zero-valued Dirichlet BCs on the internal cylindrical surface. This mixed-BC configuration couples an internal Dirichlet surface with an outer Neumann boundary, creating a challenging solution landscape.

Results. During training, NPSOLVER samples domain instances Ω from the geometry set described above and a forcing f from the forcing distribution on the fly, and is trained with the iterative physics supervision. For evaluation, we generate 10 test domain instances, each paired with 10 independent forcing fields, yielding a total of 100 test samples with ground truth solutions provided by the numerical solver. On this 3D test set, NPSOLVER achieves a mean relative L_2 error of 8.67% with an average inference time of 11.8 ms. For comparison, a supervised TRANSOLVER baseline trained with 1k labeled samples achieves a relative L_2 error of 27.22%. Visualizations of model predictions are provided in Fig. 6. Overall, these results demonstrate that NPSOLVER successfully scales to 3D irregular domains and maintains robust accuracy under mixed BCs, while substantially outperforming a representative supervised baseline.

5.3 Thermal Control on Perforated Plate

In this section, we apply NPSOLVER to a thermal boundary-control problem on a perforated electronic plate. The objective is to maintain a steady-state temperature below a safety threshold while reducing the cooling effort. We consider steady-state heat conduction on a square plate $\Omega \subset \mathbb{R}^2$ with an internal rectangular cavity. Let $u(\mathbf{x})$ denote the temperature relative to the ambient environment, governed by the equation $\nabla^2 u(\mathbf{x}) = -f(\mathbf{x})$, $\mathbf{x} \in \Omega$, where $f(\mathbf{x})$ represents volumetric heat generation from electronic components.

Geometry and BCs. We construct a family of 2D domains by subtracting a single rectangular cavity from a square domain. For each domain geometry, the cavity’s width, height, and center coordinates are randomly sampled (detailed in Appendix D.3). Controllable cooling is applied through four independently controlled Dirichlet segments on the bottom boundary, with values parameterized by a vector $\mathbf{c} = (c_1, c_2, c_3, c_4)$. All other boundaries are assigned zero-flux Neumann BCs, modeling insulated surfaces.

Results on forward problems. To address this task, NPSOLVER is trained to learn the mapping $(\Omega, \mathbf{c}, f) \rightarrow u$. During training, Ω is sampled from the geometry set described above, c_i is sampled uniformly from $[-5, 5]$, and f is sampled from a specially designed distribution (Appendix D.3) to simulate realistic heating. For evaluation, we generate 10 test domain instances, each paired with 10 independent forcing and randomized Dirichlet values \mathbf{c} , yielding a total of 100 test samples with ground-truth solutions provided by the numerical solver. On the test set, the model achieves a mean relative L_2 error of 0.58% and a peak temperature \mathbf{u}_{\max} relative error of 0.44%. The inference time is only 10.6 ms, providing the fast and accurate prediction necessary for active thermal control.

Results on control tasks. We initialize the four Dirichlet segments with $\mathbf{c} = \mathbf{0}$, i.e., no active cooling. If the predicted peak temperature $\hat{\mathbf{u}}_{\max}$ is below the prescribed threshold u_m , no control is required. Otherwise, we fix the network parameters and optimize \mathbf{c} via gradient-based updates to enforce the peak-temperature constraint while penalizing excessive cooling. Specifically, the control loss is defined as

$$L_{\text{ctrl}}(\mathbf{c}) = \text{ReLU}(\hat{\mathbf{u}}_{\max} - u_m) + \alpha \cdot \frac{1}{4} \sum_{i=1}^4 c_i^2, \quad (14)$$

where α balances constraint satisfaction and cooling effort.

We evaluate the control performance on the test set by optimizing the cooling vector \mathbf{c} over 100 iterations with a safety threshold $u_m = 25$. And we do not explicitly constrain the control range during optimization. The optimization achieved an 83% success rate in satisfying the safety constraint. On average, the peak temperature is reduced from an initial $\mathbf{u}_{\max}^{\text{init}} = 33.42$ (with $\mathbf{c} = \mathbf{0}$) to $\mathbf{u}_{\max}^{\text{opt}} = 25.31$. This significant thermal reduction is achieved with a cooling cost $\frac{1}{4} \sum_{i=1}^4 |c_i|$ of 4.47 and an average optimization time of 5.91 s per instance, demonstrating that NPSOLVER serves as an efficient differentiable surrogate for gradient-based boundary control. We further analyze the 17% failed cases and find that all failures stem from out-of-distribution control requirements: satisfying the temperature constraint requires boundary values outside the surrogate’s training range $[-5, 5]$, rather than surrogate prediction error or optimization failure. This suggests that a broader training range of \mathbf{c} may further improve robustness.

Table 3: Relative L_2 error (%) for combinations of two architectures and two training paradigms: iterative physics supervision (I.S.) and data supervision (D.S.).

Method	C4	C3	C2	C1	C0	Avg.
BA-TRANSOLVER (D.S.)	3.03	6.00	11.20	<u>11.16</u>	15.04	<u>9.29</u>
TRANSOLVER (D.S.)	5.49	8.17	12.08	15.36	18.56	11.93
TRANSOLVER (I.S.)	6.46	8.22	<u>9.44</u>	11.27	<u>13.70</u>	9.82
BA-TRANSOLVER (I.S.)	<u>4.91</u>	<u>7.07</u>	8.08	9.70	11.08	8.17

Table 4: Relative L_2 error (%) and training time (hours) for the residual supervision and iterative physics supervision with different PCG steps K .

	Residual	$K = 1$	$K = 20$	$K = 40$	$K = 80$
Rel L_2	79.59	16.80	8.12	<u>8.17</u>	8.90
Training time	10.53	10.87	11.05	11.18	11.50

As shown in Fig. 7, we visualize the heat-source field f , the initial reference temperatures \mathbf{u}^{init} , and both the reference \mathbf{u}^{opt} and NPSOLVER’s prediction $\hat{\mathbf{u}}^{\text{opt}}$ under optimized boundary values \mathbf{c} . Fig. A.3 illustrates the control loss convergence for a representative test sample. NPSOLVER reaches a loss level comparable to the numerical solver in just 0.56 s, whereas the numerical solver requires 6.20 s, representing an over 10× speedup in the optimization process. These results suggest that NPSOLVER can effectively serve as a fast surrogate in such optimization tasks, offering a favorable trade-off between computational efficiency and predictive accuracy.

5.4 Ablation Study

We conduct ablation studies on the 2D RandomBC case to evaluate the contributions of iterative physics supervision and BA-TRANSOLVER.

Architecture and supervision paradigm. We evaluate three new variants by crossing two architectures (BA-TRANSOLVER and TRANSOLVER) with two training paradigms: iterative physics supervision (I.S.) and data supervision (D.S.). Table 3 reports per-category relative L_2 errors on RandomBC. NPSOLVER, i.e., BA-TRANSOLVER (I.S.), achieves the best performance. Under data supervision, BA-TRANSOLVER outperforms vanilla TRANSOLVER, indicating that explicitly separating boundary and interior during tokenization is beneficial for the complex boundary-value problems. Furthermore, under a fixed backbone, iterative physics supervision (I.S.) consistently outperforms data supervision (D.S.), suggesting that iterative supervision acts as a stronger inductive bias than pure regression in this boundary-sensitive regime, yielding better generalization.

Impact of PCG steps in iterative supervision and residual supervision. We investigate the influence of the number of PCG steps K used to generate the iterative supervision target $\tilde{\mathbf{u}} = F_K(\hat{\mathbf{u}})$ and compare against direct residual supervision $\|\mathbf{A}\hat{\mathbf{u}} - \mathbf{b}\|$. As summarized in Table 4, residual supervision performs poorly in the complex RandomBC case. This is primarily due to the ill-conditioning of \mathbf{A} , which induces poorly scaled gradients that hinder convergence and destabilize the optimization process. In contrast, iterative

Table 5: Per-optimizer-iteration cost breakdown for residual supervision and iterative physics supervision with different PCG steps K .

	Residual	$K = 1$	$K = 20$	$K = 40$	$K = 80$
Loss time (s)	0.013	0.014	0.020	0.026	0.036
Total time (s)	0.376	0.377	0.383	0.389	0.399
Loss ratio (%)	3.46	3.71	5.22	6.68	9.02

supervision markedly improves accuracy by providing a more stable and well-scaled training signal, while introducing only a small additional training cost. A finer per-optimizer-iteration cost breakdown in Table 5 shows that even at $K = 40$, the loss computation under iterative supervision accounts for only 6.68% of each optimizer iteration, compared with 3.46% under residual supervision, indicating that the dominant training cost still comes from the network forward/backward pass rather than the PCG steps. Peak performance is achieved at an intermediate K . This trend reflects a practical trade-off: small K yields a weak correction signal that may not sufficiently guide predictions toward a numerically consistent solution, whereas overly large K can produce targets that are too aggressive relative to the current model output, increasing optimization difficulty and harming stability.

Impact of stop-gradient. We assess the necessity of stopping gradient through the K -step PCG operator $F_K(\cdot)$. Without stop-gradient, the relative L_2 error increases from 8.17% to 11.90%. This observation is consistent with Theorem C.6, which suggests that backpropagating through the truncated PCG steps can lead to more sensitive updates, while applying stop-gradient yields a more stable learning signal.

6 Conclusion

We propose NPSOLVER, a neural Poisson solver trained *without* solution labels via iterative physics supervision. Instead of relying on fully converged numerical solutions, NPSOLVER constructs self-supervision targets by applying a small, fixed number of PCG iterations to the network prediction. Our theory shows that the self-consistency residual induced by iterative supervision is a well-conditioned proxy for the solution error, and that the stop-gradient design leads to more favorable optimization dynamics. To improve generalization across domain geometries and BCs, we introduced BA-TRANSOLVER, a boundary-aware attention architecture that explicitly integrates boundary information when modeling global interactions. NPSOLVER is evaluated on a diverse suite of 2D and 3D experiments, demonstrating its ability to generalize across irregular geometries, BCs, and forcing fields, as well as its utility in a downstream thermal control application. Overall, these results show that NPSOLVER offers a favorable error–cost trade-off for complex boundary-value Poisson problems.

Limitations and Ethical Considerations

In this paper, we focus on the Poisson equation as a representative PDE setting. More broadly, our method suggests an alternative approach to constructing physics-based training objectives beyond PDE residual losses. However, its generality is not fully established

in this paper. Validating on broader PDE families and extending the current PCG/Jacobi instantiation to other Krylov solvers and stronger preconditioners remain important directions for future work. Our experiments are conducted on PDE datasets and do not involve human subjects or sensitive information.

GenAI Disclosure

The authors utilized generative AI tools to polish the language and improve the text quality. All AI-generated suggestions were thoroughly reviewed and validated by the authors.

Acknowledgments

The work is supported by the Beijing Natural Science Foundation (No. F261002) and the National Natural Science Foundation of China (No. 62276269 and No. 62506367). R.Z. would like to acknowledge the supported from the China Postdoctoral Science Foundation under Grant Number 2025M771582 and the Postdoctoral Fellowship Program of CPSF under Grant Number GZB20250408.

References

- [1] Shaojie Bai, J. Zico Kolter, and Vladlen Koltun. 2019. *Deep equilibrium models*. Curran Associates Inc., Red Hook, NY, USA.
- [2] William L. Briggs, Van Emden Henson, and Steve F. McCormick. 2000. *A Multi-grid Tutorial, Second Edition* (second ed.). Society for Industrial and Applied Mathematics. doi:10.1137/1.9780898719505
- [3] Alexandre Joel Chorin. 1968. Numerical Solution of the Navier-Stokes Equations. *Math. Comp.* 22, 104 (1968), 745–762.
- [4] Weinan E and Bing Yu. 2018. The Deep Ritz Method: A Deep Learning-Based Numerical Algorithm for Solving Variational Problems. *Communications in Mathematics and Statistics* 6, 1 (01 Mar 2018), 1–12. <https://doi.org/10.1007/s40304-018-0127-z>
- [5] Karol Gregor and Yann LeCun. 2010. Learning fast approximations of sparse coding. In *Proceedings of the 27th International Conference on International Conference on Machine Learning* (Haifa, Israel) (ICML '10). Omnipress, Madison, WI, USA, 399–406.
- [6] Tamara G Grossmann, Urszula Julia Komorowska, Jonas Latz, and Carola-Bibiane Schönlieb. 2024. Can physics-informed neural networks beat the finite element method? *IMA Journal of Applied Mathematics* 89, 1 (2024), 143–174.
- [7] XU HAN, Han Gao, Tobias Pfaff, Jian-Xun Wang, and Liping Liu. 2022. Predicting Physics in Mesh-reduced Space with Temporal Attention. In *International Conference on Learning Representations*.
- [8] M. R. Hestenes and E. Stiefel. 1952. Methods of conjugate gradients for solving linear systems. *Journal of research of the National Bureau of Standards* 49 (1952), 409–436.
- [9] Jun-Ting Hsieh, Shengjia Zhao, Stephan Eismann, Lucia Mirabella, and Stefano Ermon. 2019. Learning Neural PDE Solvers with Convergence Guarantees. In *International Conference on Learning Representations*.
- [10] J.D. Jackson. 1998. *Classical Electrodynamics*. Wiley.
- [11] Ameya D Jagtap and George Em Karniadakis. 2020. Extended physics-informed neural networks (xpinns): A generalized space-time domain decomposition based deep learning framework for nonlinear partial differential equations. *Communications in Computational Physics* 28, 5 (2020), 2002–2041.
- [12] E. Kharazmi, Z. Zhang, and G. E. Karniadakis. 2019. Variational Physics-Informed Neural Networks For Solving Partial Differential Equations. arXiv:1912.00873 [cs.NE]
- [13] Ehsan Kharazmi, Zhongqiang Zhang, and George E.M. Karniadakis. 2021. hp-VPINNs: Variational physics-informed neural networks with domain decomposition. *Computer Methods in Applied Mechanics and Engineering* 374 (2021), 113547. doi:10.1016/j.cma.2020.113547
- [14] Aditi Krishnapriyan, Amir Gholami, Shandian Zhe, Robert Kirby, and Michael W Mahoney. 2021. Characterizing possible failure modes in physics-informed neural networks. *Advances in neural information processing systems* 34 (2021), 26548–26560.
- [15] Randall J. LeVeque. 2007. *Finite Difference Methods for Ordinary and Partial Differential Equations*. Society for Industrial and Applied Mathematics. doi:10.1137/1.9780898717839
- [16] Tianyu Li, Yiye Zou, Shufan Zou, Xinghua Chang, Laiping Zhang, and Xiaogang Deng. 2024. A fully differentiable GNN-based PDE Solver: With Applications to Poisson and Navier-Stokes Equations. (2024).

- [17] Zongyi Li, Daniel Zhengyu Huang, Burigede Liu, and Anima Anandkumar. 2023. Fourier Neural Operator with Learned Deformations for PDEs on General Geometries. *Journal of Machine Learning Research* 24, 388 (2023), 1–26.
- [18] Zongyi Li, Nikola Borislavov Kovachki, Kamyar Azizzadenesheli, Burigede Liu, Kaushik Bhattacharya, Andrew Stuart, and Anima Anandkumar. 2021. Fourier Neural Operator for Parametric Partial Differential Equations. In *International Conference on Learning Representations*.
- [19] Zongyi Li, Nikola Borislavov Kovachki, Chris Choy, Boyi Li, Jean Kossaifi, Shourya Prakash Otta, Mohammad Amin Nabian, Maximilian Stadler, Christian Hundt, Kamyar Azizzadenesheli, and Anima Anandkumar. 2023. Geometry-Informed Neural Operator for Large-Scale 3D PDEs. In *Thirty-seventh Conference on Neural Information Processing Systems*.
- [20] Zijie Li, Kazem Meidani, and Amir Barati Farimani. 2023. Transformer for Partial Differential Equations' Operator Learning. *Transactions on Machine Learning Research* (2023).
- [21] Zhihao Li, Haoze Song, Di Xiao, Zhilu Lai, and Wei Wang. 2025. Harnessing Scale and Physics: A Multi-Graph Neural Operator Framework for PDEs on Arbitrary Geometries. In *Proceedings of the 31st ACM SIGKDD Conference on Knowledge Discovery and Data Mining V.1 (Toronto ON, Canada) (KDD '25)*. Association for Computing Machinery, New York, NY, USA, 729–740. doi:10.1145/3690624.3709173
- [22] Zongyi Li, Hongkai Zheng, Nikola Kovachki, David Jin, Haoxuan Chen, Burigede Liu, Kamyar Azizzadenesheli, and Anima Anandkumar. 2024. Physics-Informed Neural Operator for Learning Partial Differential Equations. *ACM / IMS J. Data Sci.* 1, 3, Article 9 (May 2024), 27 pages. doi:10.1145/3648506
- [23] Lu Lu, Pengzhan Jin, Guofei Pang, Zhongqiang Zhang, and George Em Karniadakis. 2021. Learning nonlinear operators via DeepONet based on the universal approximation theorem of operators. *Nature Machine Intelligence* 3, 3 (2021), 218–229.
- [24] Lu Lu, Xuhui Meng, Shengze Cai, Zhiping Mao, Somdatta Goswami, Zhongqiang Zhang, and George Em Karniadakis. 2022. A comprehensive and fair comparison of two neural operators (with practical extensions) based on FAIR data. *Computer Methods in Applied Mechanics and Engineering* 393 (2022), 114778. doi:10.1016/j.cma.2022.114778
- [25] Huakun Luo, Haixu Wu, Hang Zhou, Lanxiang Xing, Yichen Di, Jianmin Wang, and Mingsheng Long. 2025. Transolver++: An Accurate Neural Solver for PDEs on Million-Scale Geometries. In *International Conference on Machine Learning*.
- [26] F. Moukalled, L. Mangani, and M. Darwish. 2016. *The Finite Volume Method in Computational Fluid Dynamics: An Advanced Introduction with OpenFOAM® and Matlab*. Fluid Mechanics and its Applications, Vol. 113. Springer, Cham. doi:10.1007/978-3-319-16874-6
- [27] Ruben Ohana, Michael McCabe, Lucas Meyer, Rudy Morel, Fruzina Agocs, Miguel Beneitez, Marsha Berger, Blakesly Burkhart, Stuart Dalziel, Drummond Fielding, et al. 2024. The well: a large-scale collection of diverse physics simulations for machine learning. *Advances in Neural Information Processing Systems* 37 (2024), 44989–45037.
- [28] Suhas V Patankar. 1980. *Numerical heat transfer and fluid flow*. Hemisphere Publishing Corporation (CRC Press, Taylor & Francis Group).
- [29] Tobias Pfaff, Meire Fortunato, Alvaro Sanchez-Gonzalez, and Peter Battaglia. 2021. Learning Mesh-Based Simulation with Graph Networks. In *International Conference on Learning Representations*.
- [30] Charles R. Qi, Li Yi, Hao Su, and Leonidas J. Guibas. 2017. PointNet++: deep hierarchical feature learning on point sets in a metric space. In *Proceedings of the 31st International Conference on Neural Information Processing Systems (Long Beach, California, USA) (NIPS'17)*. Curran Associates Inc., Red Hook, NY, USA, 5105–5114.
- [31] Md Ashiqur Rahman, Zachary E Ross, and Kamyar Azizzadenesheli. 2023. U-NO: U-shaped Neural Operators. *Transactions on Machine Learning Research* (2023).
- [32] Maziar Raissi. 2018. Deep hidden physics models: deep learning of nonlinear partial differential equations. *J. Mach. Learn. Res.* 19, 1 (jan 2018), 932–955.
- [33] M. Raissi, P. Perdikaris, and G.E. Karniadakis. 2019. Physics-informed neural networks: A deep learning framework for solving forward and inverse problems involving nonlinear partial differential equations. *J. Comput. Phys.* 378 (2019), 686–707. doi:10.1016/j.jcp.2018.10.045
- [34] Ladislav Rampásek, Mikhail Galkin, Vijay Prakash Dwivedi, Anh Tuan Luu, Guy Wolf, and Dominique Beaini. 2022. Recipe for a General, Powerful, Scalable Graph Transformer. *Advances in Neural Information Processing Systems* 35 (2022).
- [35] Yousef Saad. 2003. *Iterative Methods for Sparse Linear Systems* (second ed.). Society for Industrial and Applied Mathematics. doi:10.1137/1.9780898718003
- [36] Justin Sirignano and Konstantinos Spiliopoulos. 2018. DGM: A deep learning algorithm for solving partial differential equations. *J. Comput. Phys.* 375 (2018), 1339–1364. doi:10.1016/j.jcp.2018.08.029
- [37] Alasdair Tran, Alexander Mathews, Lexing Xie, and Cheng Soon Ong. 2023. Factorized Fourier Neural Operators. In *The Eleventh International Conference on Learning Representations*.
- [38] Ulrich Trottenberg, Cornelis W. Oosterlee, and Anton Schüller. 2001. *Multigrid. Texts in Applied Mathematics*. Bd., Vol. 33. Academic Press, San Diego [u.a.]. With contributions by A. Brandt, P. Oswald and K. Stüben.
- [39] Han Wan, Qi Wang, Yuan Mi, Rui Zhang, and Hao Sun. 2026. PIMRL: Physics-Informed Multi-Scale Recurrent Learning for Burst-Sampled Spatiotemporal Dynamics. *Proceedings of the AAAI Conference on Artificial Intelligence* 40 (Mar. 2026), 1096–1104. doi:10.1609/aaai.v40i2.37080
- [40] Haixin Wang, Jiaxin LI, Anubhav Dwivedi, Kentaro Hara, and Tailin Wu. 2024. BENO: Boundary-embedded Neural Operators for Elliptic PDEs. In *The Twelfth International Conference on Learning Representations*.
- [41] Sifan Wang, Hanwen Wang, and Paris Perdikaris. 2021. Learning the solution operator of parametric partial differential equations with physics-informed DeepONets. *Science Advances* 7, 40 (2021), eabi8605. doi:10.1126/sciadv.abi8605
- [42] Sifan Wang, Xinling Yu, and Paris Perdikaris. 2022. When and why PINNs fail to train: A neural tangent kernel perspective. *J. Comput. Phys.* 449 (2022), 110768.
- [43] Haixu Wu, Huakun Luo, Haowen Wang, Jianmin Wang, and Mingsheng Long. 2024. Transolver: A Fast Transformer Solver for PDEs on General Geometries. In *International Conference on Machine Learning*.
- [44] Jeremy Yu, Lu Lu, Xuhui Meng, and George Em Karniadakis. 2022. Gradient-enhanced physics-informed neural networks for forward and inverse PDE problems. *Computer Methods in Applied Mechanics and Engineering* 393 (2022), 114823. doi:10.1016/j.cma.2022.114823
- [45] Bocheng Zeng, Qi Wang, Mengtao Yan, Yang Liu, Ruizhi Chengze, Yi Zhang, Hongsheng Liu, Zidong Wang, and Hao Sun. 2025. PhyMPGN: Physics-encoded Message Passing Graph Network for spatiotemporal PDE systems. In *The Thirteenth International Conference on Learning Representations*.
- [46] Enrui Zhang, Adar Kahana, Alena Kopaničáková, Eli Turkel, Rishikesh Ranade, Jay Pathak, and George Em Karniadakis. 2024. Blending neural operators and relaxation methods in PDE numerical solvers. *Nature Machine Intelligence* 6, 11 (01 Nov 2024), 1303–1313. doi:10.1038/s42256-024-00910-x
- [47] Rui Zhang, Qi Meng, Han Wan, Yang Liu, Zhi-Ming Ma, and Hao Sun. 2025. OmniFluids: Physics Pre-trained Modeling of Fluid Dynamics. arXiv:2506.10862 [physics.flu-dyn]
- [48] Rui Zhang, Qi Meng, Rongchan Zhu, Yue Wang, Wenlei Shi, Shihua Zhang, Zhi-Ming Ma, and Tie-Yan Liu. 2025. Monte carlo neural pde solver for learning pdes via probabilistic representation. *IEEE Transactions on Pattern Analysis and Machine Intelligence* (2025).
- [49] O.C. Zienkiewicz and R.L. Taylor. 2013. *The Finite Element Method: Its Basis and Fundamentals*. Butterworth-Heinemann.

Appendix

A FVM Discretization

We adopt a cell-centered finite-volume method (FVM) to discretize the Poisson equation on an irregular domain. As illustrated in Fig. A.1, the computational domain is partitioned into a set of non-overlapping control volumes $\{V_i\}_{i=1}^N$. The unknown u and the forcing f are stored at cell centroids $\{x_i\}$, while boundary conditions are imposed on boundary faces (grouped into boundary patches).

We consider the Poisson equation

$$\nabla^2 u(\mathbf{x}) = f(\mathbf{x}), \mathbf{x} \in \Omega, \quad (\text{A.1})$$

with boundary conditions applied on $\partial\Omega$ (Dirichlet and/or Neumann). Integrating the equation over each control volume V_i and applying the divergence theorem yield

$$\int_{V_i} \nabla^2 u dV = \int_{V_i} f dV \implies \int_{\partial V_i} \nabla u \cdot \mathbf{n} dS = \int_{V_i} f dV \quad (\text{A.2})$$

where ∂V_i is the boundary of V_i and \mathbf{n} is the outward pointing unit vector normal to ∂V_i . Let $E(i)$ denote the set of faces of cell i , $|S_e|$ the area for each face $e \in E(i)$, and $|V_i|$ the volume for each control volume V_i . The integration in Eq. A.2 can be discretized as

$$\sum_{e \in E(i)} (\nabla u \cdot \mathbf{n})_e |S_e| = f_i |V_i|, \quad (\text{A.3})$$

where f_i denotes the cell-averaged forcing in V_i .

We approximate the normal gradient using neighboring cell values. On an orthogonal mesh, a standard approximation is

$$(\nabla u \cdot \mathbf{n})_e \approx \frac{u_{N(e)} - u_i}{d_e}, \quad (\text{A.4})$$

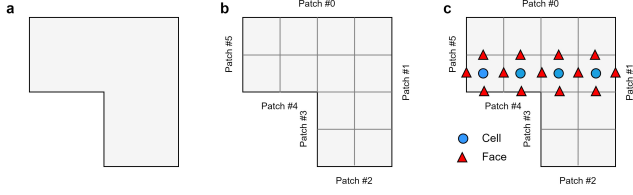


Figure A.1: (a) Computational domain. (b) FVM computational mesh (quadrilateral). (c) FVM cells and faces.

where u_i is the cell-center unknown in V_i , $u_{N(e)}$ is the neighbor-cell unknown across face e , and d_e is the projected distance along the face normal. Therefore, Eq. A.3 can be rewritten as

$$\sum_{e \in E(i)} \frac{u_{N(e)} - u_i}{d_e} |S_e| = f_i |V_i|, \quad (\text{A.5})$$

Collecting all cells leads to a sparse linear system

$$\mathbf{A}\mathbf{u} = \mathbf{b}, \quad (\text{A.6})$$

where A is the discrete Laplacian induced by the mesh and boundary treatment, and b aggregates source and boundary contributions.

For Dirichlet boundary $u(\mathbf{x}) = g_D(\mathbf{x})$ on a boundary face, the boundary value is incorporated into \mathbf{b} (and/or modifies diagonal entries) through the face flux discretization. For Neumann boundary $\frac{\partial u}{\partial \mathbf{n}} = g_N(\mathbf{x})$ on a boundary face, the prescribed flux contributes directly to the face integral. For the pure Neumann case, the system has a one-dimensional null space (solutions are defined up to an additive constant). We remove this ambiguity by imposing a reference constraint: selecting a reference location $\mathbf{x}_{\text{ref}} \in \Omega$ and enforcing $u(\mathbf{x}_{\text{ref}}) = 0$, which makes the linear system well-posed.

B Preconditioned Conjugate Gradient (PCG)

The FVM discretization yields a sparse linear system $\mathbf{A}\mathbf{u} = \mathbf{b}$. In our setting, A is large and sparse, and we solve it using the preconditioned conjugate gradient (PCG) method. PCG is an iterative Krylov-subspace solver designed for symmetric positive definite (SPD) systems, and typically achieves fast convergence when combined with an effective preconditioner.

We employ a Jacobi (diagonal) preconditioner $M = D$, where $D = \text{diag}(A)$ is the diagonal of A . Given an initial guess \mathbf{u}^0 , initialize

$$\mathbf{r}^0 = \mathbf{b} - \mathbf{A}\mathbf{u}^0, \quad \mathbf{z}^0 = M^{-1}\mathbf{r}^0, \quad \mathbf{p}^0 = \mathbf{z}^0. \quad (\text{A.7})$$

For step $k = 0, 1, 2, \dots$, PCG performs step size

$$\alpha^k = \frac{\mathbf{r}^k \cdot \mathbf{z}^k}{\mathbf{p}^k \cdot \mathbf{A}\mathbf{p}^k}, \quad (\text{A.8})$$

update the solution and residual by

$$\mathbf{u}^{k+1} = \mathbf{u}^k + \alpha^k \mathbf{p}^k, \quad \mathbf{r}^{k+1} = \mathbf{r}^k - \alpha^k \mathbf{A}\mathbf{p}^k, \quad (\text{A.9})$$

then apply the preconditioner and update the direction through

$$\mathbf{z}^{k+1} = M^{-1}\mathbf{r}^{k+1}, \quad \beta^k = \frac{\mathbf{r}^{k+1} \cdot \mathbf{z}^{k+1}}{\mathbf{r}^k \cdot \mathbf{z}^k}, \quad \mathbf{p}^{k+1} = \mathbf{z}^{k+1} + \beta^k \mathbf{p}^k \quad (\text{A.10})$$

We terminate PCG when the absolute residual norm satisfies $\|\mathbf{r}^k\|_2 \leq \epsilon$ or when a maximum iteration budget is reached. In our numerical reference solver, PCG is executed until convergence

(with $\epsilon = 1.0 \times 10^{-8}$) or until a maximum budget of 3000 iterations to produce high-quality solutions. In our iterative physics supervision, we instead run a fixed small number of PCG steps K initialized from the network prediction and use the resulting iterate as a physics-consistent supervision target.

C Proofs for Section 4

C.1 Preliminaries

We work in exact arithmetic. Let $F_K(\mathbf{u})$ denote the output of applying K steps of (preconditioned) conjugate gradients (PCG) to $\mathbf{A}\mathbf{u} = \mathbf{b}$ starting from the initial guess $\mathbf{u}_0 = \mathbf{u}$, using an SPD preconditioner M . By convention, if the current residual becomes exactly zero at some step, PCG performs no further updates and the iterate remains unchanged thereafter.

Define the self-consistency residual $\mathbf{s}_K(\mathbf{u}) := \mathbf{u} - F_K(\mathbf{u})$ and the exact solution $\mathbf{u}^* = \mathbf{A}^{-1}\mathbf{b}$ (A1). For SPD A , define $\|\mathbf{x}\|_A = \sqrt{\mathbf{x}^\top \mathbf{A}\mathbf{x}}$. Let $C = M^{-1/2}\mathbf{A}M^{-1/2}$ and $\kappa = \kappa(C)$, and define $\rho = (\kappa - 1)/(\kappa + 1) \in [0, 1)$.

LEMMA C.1 (NORM EQUIVALENCE UNDER SYMMETRIC PRECONDITIONING). *Let $\mathbf{y} = M^{1/2}\mathbf{u}$ and $\mathbf{y}^* = M^{1/2}\mathbf{u}^*$. Then \mathbf{y}^* solves $C\mathbf{y} = M^{-1/2}\mathbf{b}$, and for any \mathbf{u} ,*

$$\|\mathbf{u} - \mathbf{u}^*\|_A = \|\mathbf{y} - \mathbf{y}^*\|_C.$$

PROOF. We have $\mathbf{A}\mathbf{u} = \mathbf{b} \iff M^{-1/2}\mathbf{A}M^{-1/2}\mathbf{y} = M^{-1/2}\mathbf{b}$, i.e., $C\mathbf{y} = M^{-1/2}\mathbf{b}$. Moreover,

$$\begin{aligned} \|\mathbf{u} - \mathbf{u}^*\|_A^2 &= (\mathbf{u} - \mathbf{u}^*)^\top \mathbf{A}(\mathbf{u} - \mathbf{u}^*) \\ &= (\mathbf{y} - \mathbf{y}^*)^\top M^{-1/2}\mathbf{A}M^{-1/2}(\mathbf{y} - \mathbf{y}^*) \\ &= \|\mathbf{y} - \mathbf{y}^*\|_C^2. \end{aligned}$$

□

LEMMA C.2 (KANTOROVICH INEQUALITY). *Let C be SPD with eigenvalues in $[\lambda_{\min}, \lambda_{\max}]$ and $\kappa = \lambda_{\max}/\lambda_{\min}$. Then for any nonzero \mathbf{x} ,*

$$(\mathbf{x}^\top C\mathbf{x})(\mathbf{x}^\top C^{-1}\mathbf{x}) \leq \frac{(\lambda_{\max} + \lambda_{\min})^2}{4\lambda_{\max}\lambda_{\min}} (\mathbf{x}^\top \mathbf{x})^2 = \frac{(\kappa + 1)^2}{4\kappa} (\mathbf{x}^\top \mathbf{x})^2.$$

PROOF. Diagonalize $C = \mathbf{Q}\mathbf{\Lambda}\mathbf{Q}^\top$ and let $\mathbf{y} = \mathbf{Q}^\top \mathbf{x}$. Write $S = \sum_i y_i^2 = \mathbf{x}^\top \mathbf{x}$ and weights $w_i = y_i^2/S$ so that $\sum_i w_i = 1$. Then

$$\mathbf{x}^\top C\mathbf{x} = S \sum_i w_i \lambda_i, \quad \mathbf{x}^\top C^{-1}\mathbf{x} = S \sum_i w_i \lambda_i^{-1}.$$

For each $\lambda_i \in [\lambda_{\min}, \lambda_{\max}]$ we have $(\lambda_i - \lambda_{\min})(\lambda_i - \lambda_{\max}) \leq 0$, i.e. $\lambda_i^2 - (\lambda_{\min} + \lambda_{\max})\lambda_i + \lambda_{\min}\lambda_{\max} \leq 0$. Dividing by $\lambda_i > 0$ gives

$$\lambda_i + \frac{\lambda_{\min}\lambda_{\max}}{\lambda_i} \leq \lambda_{\min} + \lambda_{\max}.$$

Averaging w.r.t. w_i yields

$$\sum_i w_i \lambda_i + \lambda_{\min}\lambda_{\max} \sum_i w_i \lambda_i^{-1} \leq \lambda_{\min} + \lambda_{\max}.$$

By AM–GM inequality,

$$\begin{aligned} 2\sqrt{\lambda_{\min}\lambda_{\max}} \left(\sum_i w_i \lambda_i \right) \left(\sum_i w_i \lambda_i^{-1} \right) &\leq \sum_i w_i \lambda_i + \lambda_{\min}\lambda_{\max} \sum_i w_i \lambda_i^{-1} \\ &\leq \lambda_{\min} + \lambda_{\max}. \end{aligned}$$

Squaring and rearranging proves

$$\left(\sum_i w_i \lambda_i\right) \left(\sum_i w_i \lambda_i^{-1}\right) \leq \frac{(\lambda_{\min} + \lambda_{\max})^2}{4\lambda_{\min}\lambda_{\max}}.$$

Multiplying by S^2 completes the proof. \square

LEMMA C.3 (ONE-STEP STEEPEST DESCENT CONTRACTION). *Consider solving $C\mathbf{y} = \mathbf{d}$ with SPD C by steepest descent with exact line search:*

$$\mathbf{y}^+ = \mathbf{y} + \alpha \mathbf{r}, \quad \mathbf{r} = \mathbf{d} - C\mathbf{y}, \quad \alpha = \frac{\mathbf{r}^\top \mathbf{r}}{\mathbf{r}^\top C \mathbf{r}}.$$

Let $\mathbf{e} = \mathbf{y} - \mathbf{y}^*$ where $\mathbf{y}^* = C^{-1}\mathbf{d}$. Then

$$\|\mathbf{e}^+\|_C \leq \rho \|\mathbf{e}\|_C, \quad \rho = \frac{\kappa(C) - 1}{\kappa(C) + 1}.$$

PROOF. Since $\mathbf{r} = \mathbf{d} - C\mathbf{y} = -C(\mathbf{y} - \mathbf{y}^*) = -C\mathbf{e}$, the update gives $\mathbf{e}^+ = \mathbf{e} - \alpha C\mathbf{e}$. Expanding the C -norm,

$$\|\mathbf{e}^+\|_C^2 = (\mathbf{e} - \alpha C\mathbf{e})^\top C(\mathbf{e} - \alpha C\mathbf{e}) = \|\mathbf{e}\|_C^2 - \frac{(\mathbf{r}^\top \mathbf{r})^2}{\mathbf{r}^\top C \mathbf{r}}.$$

Also note $\mathbf{r}^\top C^{-1}\mathbf{r} = \mathbf{e}^\top C\mathbf{e} = \|\mathbf{e}\|_C^2$. Therefore

$$\frac{\|\mathbf{e}^+\|_C^2}{\|\mathbf{e}\|_C^2} = 1 - \frac{(\mathbf{r}^\top \mathbf{r})^2}{(\mathbf{r}^\top C \mathbf{r})(\mathbf{r}^\top C^{-1}\mathbf{r})}.$$

By Lemma C.2,

$$\begin{aligned} (\mathbf{r}^\top C \mathbf{r})(\mathbf{r}^\top C^{-1}\mathbf{r}) &\leq \frac{(\kappa + 1)^2}{4\kappa} (\mathbf{r}^\top \mathbf{r})^2 \\ \Rightarrow \frac{(\mathbf{r}^\top \mathbf{r})^2}{(\mathbf{r}^\top C \mathbf{r})(\mathbf{r}^\top C^{-1}\mathbf{r})} &\geq \frac{4\kappa}{(\kappa + 1)^2}. \end{aligned}$$

Hence

$$\frac{\|\mathbf{e}^+\|_C^2}{\|\mathbf{e}\|_C^2} \leq 1 - \frac{4\kappa}{(\kappa + 1)^2} = \left(\frac{\kappa - 1}{\kappa + 1}\right)^2 = \rho^2,$$

which implies $\|\mathbf{e}^+\|_C \leq \rho \|\mathbf{e}\|_C$. \square

LEMMA C.4 (PCG- K CONTRACTION IN THE ENERGY NORM). *Assume A1–A2. Then for any initial guess \mathbf{u} ,*

$$\|F_K(\mathbf{u}) - \mathbf{u}^*\|_A \leq \rho^K \|\mathbf{u} - \mathbf{u}^*\|_A.$$

PROOF. Under SPD M , standard symmetrically-preconditioned CG (PCG) on (A, M) is equivalent to applying (unpreconditioned) CG to the SPD system $C\mathbf{y} = M^{-1/2}\mathbf{b}$ in the variable $\mathbf{y} = M^{1/2}\mathbf{u}$. CG produces the C -norm optimal error over the K -step Krylov subspace; in particular, its error after K iterations is no worse than that of K steps of steepest descent with exact line search. By Lemma C.3, steepest descent contracts the C -norm error by at most ρ per step, hence after K steps:

$$\|\mathbf{y}_K - \mathbf{y}^*\|_C \leq \rho^K \|\mathbf{y}_0 - \mathbf{y}^*\|_C.$$

Finally apply Lemma C.1 to translate back to A -energy norms: $\|\mathbf{y}_K - \mathbf{y}^*\|_C = \|F_K(\mathbf{u}) - \mathbf{u}^*\|_A$ and $\|\mathbf{y}_0 - \mathbf{y}^*\|_C = \|\mathbf{u} - \mathbf{u}^*\|_A$. \square

C.2 Proof of Fixed-point Consistency

THEOREM C.5 (FIXED-POINT CONSISTENCY). *Assume A1–A2 and $K \geq 1$. Then for any $\mathbf{u} \in \mathbb{R}^N$,*

$$F_K(\mathbf{u}) = \mathbf{u} \iff \mathbf{A}\mathbf{u} = \mathbf{b}.$$

PROOF. (\Rightarrow) Suppose $\mathbf{A}\mathbf{u} = \mathbf{b}$. Then the initial residual is $\mathbf{r}_0 = \mathbf{b} - \mathbf{A}\mathbf{u} = \mathbf{0}$. By the definition of PCG and our convention, no further updates are performed, hence $F_K(\mathbf{u}) = \mathbf{u}$.

(\Leftarrow) Suppose $\mathbf{A}\mathbf{u} \neq \mathbf{b}$, i.e. $\mathbf{r}_0 = \mathbf{b} - \mathbf{A}\mathbf{u} \neq \mathbf{0}$. In PCG, the first preconditioned residual is $\mathbf{z}_0 = M^{-1}\mathbf{r}_0 \neq \mathbf{0}$ (because M is nonsingular SPD), and the first search direction is $\mathbf{p}_0 = \mathbf{z}_0$. The first step size is

$$\alpha_0 = \frac{\mathbf{r}_0^\top \mathbf{z}_0}{\mathbf{p}_0^\top \mathbf{A} \mathbf{p}_0}.$$

Since M and A are SPD, $\mathbf{r}_0^\top \mathbf{z}_0 = \mathbf{r}_0^\top M^{-1}\mathbf{r}_0 > 0$ and $\mathbf{p}_0^\top \mathbf{A} \mathbf{p}_0 > 0$, hence $\alpha_0 > 0$. Therefore, the first iterate updates as $\mathbf{u}_1 = \mathbf{u} + \alpha_0 \mathbf{p}_0 \neq \mathbf{u}$. When $K \geq 1$, we have $\mathbf{u}_K = \mathbf{u} + \sum_{i=0}^{K-1} \alpha_i \mathbf{p}_i$. If $\mathbf{u}_K = \mathbf{u}$, then $\sum_{i=0}^{K-1} \alpha_i \mathbf{p}_i = \mathbf{0}$. Left-multiplying by $\mathbf{p}_0^\top \mathbf{A}$ and using the A -conjugacy $\mathbf{p}_0^\top \mathbf{A} \mathbf{p}_i = 0$ for $i \geq 1$, we obtain $0 = \alpha_0 \mathbf{p}_0^\top \mathbf{A} \mathbf{p}_0$, contradicting $\alpha_0 > 0$ and SPD of A . Hence $\mathbf{u}_K \neq \mathbf{u}$. Therefore, $F_K(\mathbf{u}) = \mathbf{u}$ implies $\mathbf{r}_0 = \mathbf{0}$, i.e. $\mathbf{A}\mathbf{u} = \mathbf{b}$. \square

C.3 Proof of Stop-gradient Contraction

THEOREM C.6 (STOP-GRADIENT CONTRACTION). *Assume A1–A2 and $K \geq 1$. Consider the iteration $\mathbf{u}_{t+1} = \mathbf{u}_t - \eta \mathbf{s}_K(\mathbf{u}_t) = (1 - \eta)\mathbf{u}_t + \eta F_K(\mathbf{u}_t)$ with $\eta \in (0, 1]$. Let $\mathbf{e}_t = \mathbf{u}_t - \mathbf{u}^*$. Then*

$$\|\mathbf{e}_{t+1}\|_A \leq ((1 - \eta) + \eta \rho^K) \|\mathbf{e}_t\|_A = (1 - \eta(1 - \rho^K)) \|\mathbf{e}_t\|_A.$$

PROOF. Using $\mathbf{u}^* = F_K(\mathbf{u}^*)$ and the update definition,

$$\begin{aligned} \mathbf{e}_{t+1} = \mathbf{u}_{t+1} - \mathbf{u}^* &= (1 - \eta)(\mathbf{u}_t - \mathbf{u}^*) + \eta(F_K(\mathbf{u}_t) - \mathbf{u}^*) \\ &= (1 - \eta)\mathbf{e}_t + \eta(F_K(\mathbf{u}_t) - \mathbf{u}^*). \end{aligned}$$

Taking A -norms and applying the triangle inequality gives

$$\|\mathbf{e}_{t+1}\|_A \leq (1 - \eta)\|\mathbf{e}_t\|_A + \eta\|F_K(\mathbf{u}_t) - \mathbf{u}^*\|_A.$$

Finally apply Lemma C.4 to bound $\|F_K(\mathbf{u}_t) - \mathbf{u}^*\|_A \leq \rho^K \|\mathbf{e}_t\|_A$, yielding the claim. \square

C.4 Proof of the Error-proxy Theorem

THEOREM C.7 (SELF-CONSISTENCY RESIDUAL AS AN ERROR PROXY). *Assume A1–A2 and $K \geq 1$. Then for any \mathbf{u} ,*

$$(1 - \rho^K) \|\mathbf{u} - \mathbf{u}^*\|_A \leq \|\mathbf{s}_K(\mathbf{u})\|_A \leq (1 + \rho^K) \|\mathbf{u} - \mathbf{u}^*\|_A.$$

Furthermore, letting $\mathbf{r}(\mathbf{u}) = \mathbf{A}\mathbf{u} - \mathbf{b}$, we have

$$\lambda_{\min}(\mathbf{A}) \|\mathbf{u} - \mathbf{u}^*\|_A \leq \|\mathbf{r}(\mathbf{u})\|_A \leq \lambda_{\max}(\mathbf{A}) \|\mathbf{u} - \mathbf{u}^*\|_A.$$

PROOF. Let $\mathbf{e} = \mathbf{u} - \mathbf{u}^*$ and $\mathbf{e}_K = F_K(\mathbf{u}) - \mathbf{u}^*$. Then $\mathbf{s}_K(\mathbf{u}) = \mathbf{u} - F_K(\mathbf{u}) = \mathbf{e} - \mathbf{e}_K$. By the triangle inequality and Lemma C.4,

$$\|\mathbf{s}_K(\mathbf{u})\|_A \leq \|\mathbf{e}\|_A + \|\mathbf{e}_K\|_A \leq (1 + \rho^K) \|\mathbf{e}\|_A.$$

Similarly, by the reverse triangle inequality,

$$\|\mathbf{s}_K(\mathbf{u})\|_A \geq \|\|\mathbf{e}\|_A - \|\mathbf{e}_K\|_A\| \geq (1 - \rho^K) \|\mathbf{e}\|_A.$$

This proves the first inequality.

For the residual bound, note $\mathbf{r}(\mathbf{u}) = \mathbf{A}\mathbf{u} - \mathbf{b} = \mathbf{A}(\mathbf{u} - \mathbf{u}^*) = \mathbf{A}\mathbf{e}$. Then

$$\|\mathbf{r}(\mathbf{u})\|_A^2 = \mathbf{r}^\top \mathbf{A} \mathbf{r} = (\mathbf{A}\mathbf{e})^\top \mathbf{A} (\mathbf{A}\mathbf{e}) = \mathbf{e}^\top \mathbf{A}^3 \mathbf{e}.$$

Let the eigenvalues of A lie in $[\lambda_{\min}(A), \lambda_{\max}(A)]$. In an eigenbasis of A , each component satisfies $\lambda_{\min}(A)^2 \lambda_i \leq \lambda_i^3 \leq \lambda_{\max}(A)^2 \lambda_i$, which implies the matrix inequality $\lambda_{\min}(A)^2 A \preceq A^3 \preceq \lambda_{\max}(A)^2 A$. Therefore,

$$\lambda_{\min}(A)^2 \mathbf{e}^\top A \mathbf{e} \leq \mathbf{e}^\top A^3 \mathbf{e} \leq \lambda_{\max}(A)^2 \mathbf{e}^\top A \mathbf{e}.$$

Taking square roots yields

$$\lambda_{\min}(A) \|\mathbf{e}\|_A \leq \|\mathbf{r}(\mathbf{u})\|_A \leq \lambda_{\max}(A) \|\mathbf{e}\|_A.$$

□

C.5 Derivation for the Local Expansions in Remark

Assume F_K is Fréchet differentiable at \mathbf{u}^* with Jacobian $J = \nabla F_K(\mathbf{u}^*)$. For $\mathbf{u} = \mathbf{u}^* + \mathbf{e}$ and small \mathbf{e} ,

$$\begin{aligned} F_K(\mathbf{u}) &= F_K(\mathbf{u}^* + \mathbf{e}) = \mathbf{u}^* + J\mathbf{e} + O(\|\mathbf{e}\|_2^2), \\ s_K(\mathbf{u}) &= \mathbf{u} - F_K(\mathbf{u}) = (I - J)\mathbf{e} + O(\|\mathbf{e}\|_2^2). \end{aligned}$$

For the stop-gradient update $\mathbf{u}^+ = \mathbf{u} - \eta s_K(\mathbf{u})$,

$$\mathbf{e}^+ = \mathbf{u}^+ - \mathbf{u}^* = \mathbf{e} - \eta(I - J)\mathbf{e} + O(\|\mathbf{e}\|_2^2) = ((1 - \eta)I + \eta J)\mathbf{e} + O(\|\mathbf{e}\|_2^2).$$

For the full-gradient update on $\phi(\mathbf{u}) = \frac{1}{2} \|s_K(\mathbf{u})\|_2^2$, $\nabla \phi(\mathbf{u}) = (\nabla s_K(\mathbf{u}))^\top s_K(\mathbf{u})$ and $\nabla s_K(\mathbf{u}^*) = I - J$, hence

$$\begin{aligned} \nabla \phi(\mathbf{u}) &= (I - J)^\top (I - J)\mathbf{e} + O(\|\mathbf{e}\|_2^2), \\ \mathbf{e}^+ &= (I - \eta(I - J)^\top (I - J))\mathbf{e} + O(\|\mathbf{e}\|_2^2). \end{aligned}$$

D More Details in Experiments

The hyperparameters about the number of model parameters, epochs, batch size, and learning rate for training NPSOLVER and baselines across different tasks are summarized in Table A.1. The default setting of PCG steps K for NPSOLVER is 40. All source code and data will be made available after peer review.

D.1 2D Generalization under Different BCs

Geometry. Following BENO [40], we construct a corner-removed square family with five categories, denoted as C_k , where $k \in \{0, \dots, 4\}$ is the number of removed rectangular corners (C_0 corresponds to the intact square). The base domain is defined on $[0, L]^2$ with $L = 2\pi$ and a base resolution 128×128 . For each domain geometry, the width and height of the removed corner rectangles are sampled independently from a uniform distribution over $[0.1L, 0.4L]$. To evaluate both in-distribution and out-of-distribution generalization ability, we *train* the model only on the most irregular category C_4 and *test* it on all categories C_0 - C_4 . We prepare 100 domain instances forming the training geometry set and 10 domain instances per category forming the testing geometry set. The average number of cells per category is summarized in Table A.2.

Forcing distribution. Given 3D spatial coordinates $\{\mathbf{x}_n\}_{n=1}^N$ with $\mathbf{x}_n = (x_n, y_n, z_n)$ at cell centroids of control volumes $\{V_n\}_{n=1}^N$, where $z_n = 0$ for 2D, define the frequency index set

$$\mathcal{K} = \{(i, j, k) \mid i, j, k \in \{0, 1, \dots, M-1\}\},$$

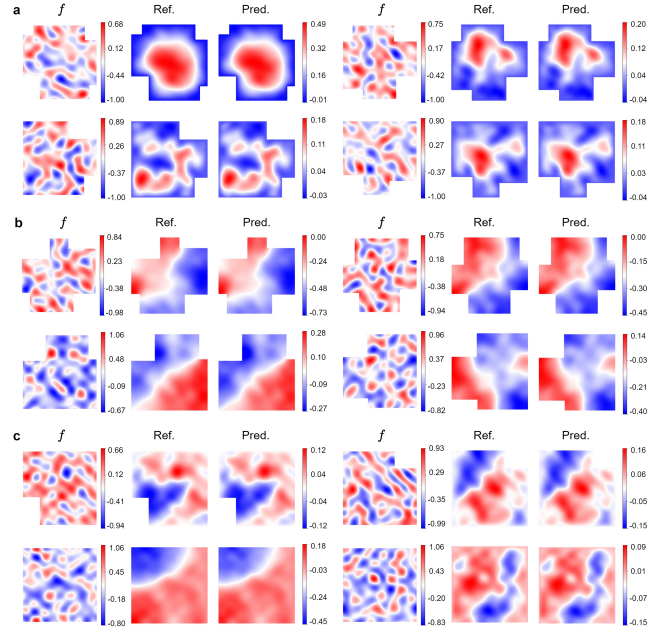


Figure A.2: Visualization of NPSOLVER's predictions for representative samples. (a) All-Dirichlet case (C4 and C2). (b) All-Neumann case (C4 and C2). (c) RandomBC case (C1 and C0).

and let $A_{ijk}, B_{ijk} \stackrel{\text{i.i.d.}}{\sim} \mathcal{N}(0, 1)$ for $(i, j, k) \in \mathcal{K}$, and $c \sim \mathcal{N}(-1, 1)$. For each centroid \mathbf{x}_n , define the phase

$$\phi_{ijk}(\mathbf{x}_n) = \left(i - \left\lfloor \frac{M}{2} \right\rfloor\right) x_n + \left(j - \left\lfloor \frac{M}{2} \right\rfloor\right) y_n + \left(k - \left\lfloor \frac{M}{2} \right\rfloor\right) z_n,$$

and construct

$$W(\mathbf{x}_n) = \sum_{i=0}^{M-1} \sum_{j=0}^{M-1} \sum_{k=0}^{M-1} \left(A_{ijk} \sin(\phi_{ijk}(\mathbf{x}_n)) + B_{ijk} \cos(\phi_{ijk}(\mathbf{x}_n)) \right).$$

Add the bias term:

$$f_0(\mathbf{x}_n) = W(\mathbf{x}_n) + c.$$

The returned field is

$$f(\mathbf{x}_n) = \frac{f_0(\mathbf{x}_n)}{\max_{1 \leq m \leq N} |f_0(\mathbf{x}_m)| + \varepsilon}.$$

In practice, we choose $M = 10$ to ensure sufficient spectral richness. For the pure zero-flux Neumann case, in order to satisfy the compatibility condition $\int_{\Omega} f = 0$, we normalize f by

$$\bar{f} = \frac{\sum_{n=1}^N f(\mathbf{x}_n) |V_n|}{\sum_{n=1}^N |V_n|}, \quad f(\mathbf{x}_n)^{\text{norm}} = f(\mathbf{x}_n) - \bar{f},$$

where $|V_i|$ is the volume for each control volume V_i .

For evaluation, we pair 50 test domain instances (10 per category) with 10 independent forcing realizations each. This yields 100 test samples per category and 500 total test samples per case, with ground-truth solutions provided by the numerical solver.

Table A.1: The number of model parameters, epochs, batch size, and learning rate for training NPSOLVER across different tasks.

Task	Method	Params.	Epochs	Batch size	LR
2D Dirichlet	PI-DEEPONET	3.6M	400	100	0.001
	PINO	3.5M	400	8	0.001
	PINN	0.2M	11000	1	0.001
	NPSOLVER	3.6M	400	8	0.001
2D Neumann	PI-DEEPONET	3.6M	600	100	0.0005
	PINO	3.5M	600	8	0.0005
	PINN	0.2M	11000	1	0.0005
	NPSOLVER	3.6M	600	8	0.0005
2D RandomBC	TRANSOLVER	3.5M	1000	8	0.0005
	TRANSOLVER++	2.9M	1000	8	0.0005
	MGN	2.2M	1000	4	0.0005
	GPS	2.6M	1000	4	0.0005
	POINTNET++	3.5M	1000	8	0.0005
	BENO	3.4M	1000	6	0.0005
	NPSOLVER	3.6M	1000	8	0.0005
3D	TRANSOLVER	4.7M	400	1	0.0005
	NPSOLVER	4.9M	400	1	0.0005
Control	NPSOLVER	3.6M	1000	8	0.0005

Implementation details of baselines. To ensure a fair and comprehensive comparison, we adapt three representative physics-informed baselines to our irregular domain and variable BC settings. All models, including NPSOLVER, are trained using identical optimization protocols: the Adam optimizer with a OneCycle learning-rate schedule for an equal number of epochs.

- **PI-DEEPONET:** The standard branch net architecture implicitly assumes a fixed sensor configuration, making it incompatible with irregular domains of varying node counts. To address this, we interpolate the irregular input fields onto a fixed 128×128 Cartesian grid to serve as the branch net input. The trunk net then queries coordinates from the original irregular mesh.
- **PINO:** Since the FNO backbone requires regular grids, we perform bi-directional interpolation and masking between the irregular physical domain and a latent regular grid for the network’s input and output. Crucially, the finite-volume equation residuals are still computed on the original irregular mesh to maintain physical consistency during training.
- **PINN:** Unlike the models above, PINN is optimized from scratch for each test sample. The optimization follows a two-stage strategy: an initial 1,000 Adam iterations for global search, followed by 10,000 L-BFGS iterations to ensure fine-scale convergence. While providing a high-accuracy reference, this process incurs a prohibitive computational cost during inference. We evaluate PINN on a representative subset by selecting three samples from each category. The average performance across these selections is reported as the final estimate for the category.
- **Data-driven baselines (TRANSOLVER, TRANSOLVER++, MGN, GPS, POINTNET++, BENO):** These data-driven baselines are inherently suited for modeling boundary-value problems on irregular geometries. For a fair comparison, all models are trained for the

Table A.2: Average number of cells per category in the 2D computational domain.

	C4	C3	C2	C1	C0
Avg. Cells	12567	13806	14678	15245	16384

same number of epochs as NPSOLVER. Due to GPU memory constraints, the batch size is set to 8 for TRANSOLVER, TRANSOLVER++, POINTNET++, and NPSOLVER, 4 for MGN and GPS, and 6 for BENO. Notably, the number of iterations per epoch for NPSOLVER is fixed at 100, whereas for other models, it scales with the dataset size (e.g., 125 iterations per epoch for 1k samples with a batch size of 8). This configuration intentionally favors the data-driven baselines by granting them a higher frequency of parameter updates, further underscoring the efficiency of our approach.

D.2 3D Poisson on Cube-with-Cylindrical-Hole

Geometry and BCs. We construct a 3D domain family by subtracting a cylindrical cavity from a cube $[0, L]^3$ with $L = 2\pi$, discretized at a base resolution of 48^3 . The cylinder’s diameter d is sampled uniformly from $[0.1L, 0.3L]$, and its center is randomized such that the cylinder remains fully contained within the cube. We prepare 40 domain instances forming the training geometry set and 10 domain instances forming the testing geometry set. The average number of cells of the testing geometry set is about 100,420. Regarding BCs, we impose zero-flux Neumann BCs on the outer cube surfaces and Dirichlet BCs with zero value on the internal

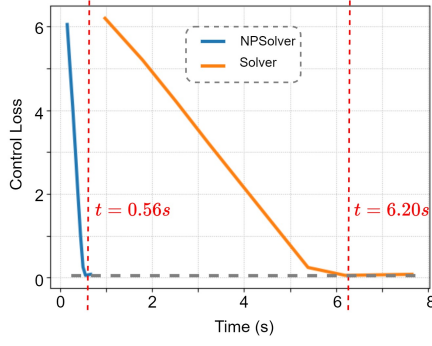


Figure A.3: Control-loss convergence curve for a representative sample in the thermal control task.

cylindrical surface. This mixed-BC configuration couples an internal Dirichlet surface with an outer Neumann boundary, creating a challenging solution landscape.

Forcing distribution. The distribution of the forcing field in 3D is identical to that used in 2D.

For evaluation, we pair 10 test domain instances with 10 independent forcing realizations each, yielding 100 test samples with ground-truth solutions provided by the numerical solver.

D.3 Thermal Control on Perforated Plate

Geometry and BCs. We construct a family of 2D domains by subtracting a single rectangular cavity from a square domain $[0, L]^2$ with $L = 2\pi$, discretized at a base resolution of 128^2 . For each domain geometry, the cavity’s width and height are sampled independently from $[0.1L, 0.4L]$, with its center sampled such that the hole remains fully contained within the square. We prepare 100 domain instances forming the training geometry set and 10 domain instances forming the testing geometry set. The average number of cells of the testing geometry set is about 15,080. Controllable cooling is applied through four independently controlled Dirichlet segments on the bottom boundary, with values parameterized by a vector $\mathbf{c} = (c_1, c_2, c_3, c_4)$. All other boundaries are assigned zero-flux Neumann BCs, modeling insulated surfaces.

Forcing distribution. To simulate randomly distributed heating elements, the source term f is sampled from the specially designed distribution, generated as a superposition of localized Gaussian “hot spots” with randomized centers, amplitudes, and spatial spreads. Given 2D spatial coordinates $\{\mathbf{x}_i\}_{i=1}^n$ with $\mathbf{x}_i = (x_i, y_i) \in [0, L]^2$, we generate a nonnegative heat-source field $f : \{\mathbf{x}_i\} \rightarrow \mathbb{R}_{\geq 0}$ as a sum of K Gaussian hot spots:

- 1) Number of hot spots:

$$K \sim \text{Unif}\{K_{\min}, K_{\max}\}.$$

- 2) Hot-spot centers: we sample K indices $\{c_k\}_{k=1}^K$ i.i.d. from $\{1, \dots, n\}$, and set

$$\boldsymbol{\mu}_k = \mathbf{x}_{c_k} = (\mu_{k,x}, \mu_{k,y}).$$

- 3) Amplitudes and widths:

$$A_k \sim \text{Unif}(a_{\min}, a_{\max}), \quad s_k \sim \text{Unif}(s_{\min}, s_{\max}).$$

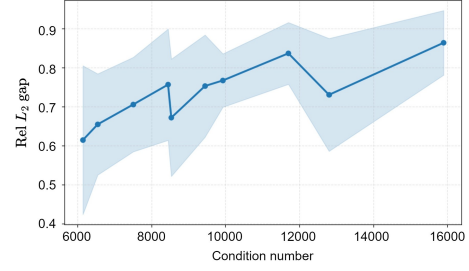


Figure A.4: Relationship between the estimated condition number and the relative L_2 error gap between residual supervision and iterative supervision on C4.

and we use isotropic widths

$$\sigma_{k,x} = \sigma_{k,y} = s_k.$$

- 4) Unnormalized field: for each point $\mathbf{x}_i = (x_i, y_i)$,

$$f_0(\mathbf{x}_i) = \sum_{k=1}^K A_k \exp\left(-\frac{1}{2} \left(\frac{x_i - \mu_{k,x}}{\sigma_{k,x} + \varepsilon}\right)^2 - \frac{1}{2} \left(\frac{y_i - \mu_{k,y}}{\sigma_{k,y} + \varepsilon}\right)^2\right), \quad \varepsilon = 10^{-8}.$$

- 5) Mean-power scaling: define the sample mean

$$\bar{f}_0 = \frac{1}{n} \sum_{i=1}^n f_0(\mathbf{x}_i).$$

Then the returned heat-source field is scaled:

$$f(\mathbf{x}_i) = f_0(\mathbf{x}_i) \cdot \frac{1}{\bar{f}_0 + \varepsilon}.$$

In practice, we choose $K_{\min} = 2, K_{\max} = 6, a_{\min} = 0.5, a_{\max} = 2.0, s_{\min} = 0.02L, s_{\max} = 0.08L, L = 2\pi$ to produce spatially sparse, inhomogeneous sources that resemble heat injection from discrete components.

For evaluation, we pair 10 test domain instances with 10 independent forcing and randomized Dirichlet values \mathbf{c} , yielding a total of 100 test samples with ground-truth solutions provided by the numerical solver.

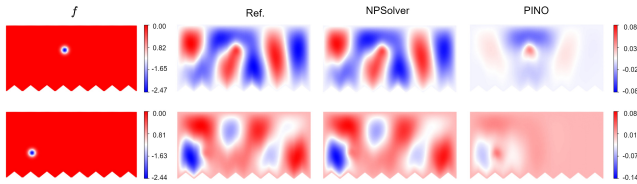
E Additional Analysis and Experiments

Condition-number analysis. We further analyze the relationship between the estimated condition number and the performance gap between residual supervision and iterative supervision. Since the model is trained on C4 and tested on C0–C4, cross-category comparisons mix conditioning and OOD geometry generalization. We therefore restrict this analysis to samples within the C4 family. As shown in Fig A.4, the relative L_2 gap shows an overall increasing trend with the estimated condition number. The Pearson correlation between the estimated condition number and the relative L_2 gap is 0.84, supporting our claim that residual supervision is more sensitive to ill-conditioning while iterative supervision provides a better-scaled signal.

Variable-coefficient Poisson equation. We add experiments on the variable-coefficient Poisson equation $\nabla \cdot (D(\mathbf{x})\nabla u(\mathbf{x})) = f(\mathbf{x})$ in the All-Dirichlet BCs setting. Following the setup in Section 5.1, the model is trained on the most irregular category C4 and tested on C0–C4, where it must simultaneously generalize across the geometry domain Ω , the coefficient field $D(\mathbf{x})$, and the forcing

Table A.3: Relative L_2 errors (%) on variable-coefficient Poisson equation in the All-Dirichlet BCs.

Method	C4	C3	C2	C1	C0
PINO	25.18	24.66	29.09	30.73	32.88
NPSOLVER	1.83	3.07	3.82	4.75	5.50

**Figure A.5: Visualization of models' predictions for representative samples.**

field $f(x)$. As shown in Table A.3, NPSOLVER outperforms PINO by a large margin on all test categories, confirming that our framework also works well for variable-coefficient Poisson equations.

Helmholtz equation. We further broaden the empirical evaluation with the 2D Helmholtz equation, following The Well Benchmark [27]. Specifically, we consider $\Delta u + \omega^2 u = -\delta_{x_0}$ on a rectangular region with a jagged lower boundary, whose bounding box is $[0, 2\pi] \times [0, \pi]$ and discretized with approximately 128×64 nodes and Dirichlet BCs. The task requires generalization across varying point-source right-hand sides $-\delta_{x_0}$. We train NPSOLVER in the same label-free manner via iterative physics supervision and compare it with PINO as a representative baseline. On this Helmholtz case, NPSolver achieves a relative L_2 error of 3.37%, whereas PINO obtains 87.60%. A representative prediction snapshot is shown in Fig. A.5. This experiment provides additional evidence that the core iterative supervision idea is not limited to the exact Poisson problem considered in the main paper.